Numerical criterion for incipient separation of turbulent flows as inferred by RANS

Dawei Lu

A thesis
submitted in partial fulfillment of the
requirements for the degree of

Master of Science in Aeronautics & Astronautics

University of Washington

2019

Committee:

Antonino Ferrante

Owen Williams

Program Authorized to Offer Degree:
Aeronautics & Astronautics

University of Washington

Abstract

Numerical criterion for incipient separation of turbulent flows
as inferred by RANS

Dawei Lu

Chair of the Supervisory Committee:
Associate Professor Antonino Ferrante
Aeronautics & Astronautics

Simulations of turbulent flows based on the Reynolds-averaged Navier-Stokes (RANS) equations are widely used for engineering applications and are computationally less expensive than other numerical simulations such as large-eddy or direct numerical simulations. We performed RANS simulations over smooth curved surfaces under adverse pressure gradient using a one-equation turbulence model and without wall-functions (i.e., the grid is fine enough to reach the viscous sublayer). First, by investigating the effect of inflow boundary condition, domain size and grid refinement, we assessed the best practices for RANS simulations. Next, we validated the RANS by comparing the results with published experimental measurements. Further, the sensitivity of turbulent flow to the degree of severity of the adverse pressure gradient is investigated by testing different curved ramp geometries, by varying the ramp slope and curvature distribution. Our results show that the key parameter to determine flow separation is the maximum slope of the ramp normalized by the non-dimensional ramp height over its streamwise length, and the location of the maximum curvature has an effect on the magnitude of skin-friction coefficient near the onset of ramp. Lastly, a numerical criterion for incipient separation as inferred by RANS is proposed. Based on this criterion, a new approach is demonstrated to examine flow separation that depends only on the ramp height-to-length ratio, normalized maximum slope and Reynolds number for the range of $2 \times 10^5 \leq Re_L \leq 8 \times 10^5$ simulated via RANS.

TABLE OF CONTENTS

LIST OF FIGURES

LIST OF TABLES

NOMENCLATURE

Greek

α	constant of criterion for incipient separation
β	constant of criterion for incipient separation
δ	boundary layer thickness; also, Kronecker delta δ_{ij}
δ^*	displacement thickness
ϵ	error of flow property for calculating GCI
γ	stretching factor
κ	longitudinal curvature of surface definition
μ	dynamic viscosity
ν	kinematic viscosity
ν_{eff}	effective viscosity
ν_t	turbulent viscosity
ϕ	flow property for calculating grid convergence index (GCI)
ρ	density
σ	ratio of flat downstream height to flat upstream height; also, L_2 norm
τ_w	wall shear stress

τ_{ij} stress tensor

θ momentum thickness

$\tilde{\nu}$ modified turbulent viscosity

ξ DARPA Suboff geometry variable

ζ uniform grid in z direction

Roman

ΔA cell area

$\widetilde{h}$ ramp height-to-length ratio $(= h/L)$

$\widetilde{z'}$ normalized slope $(= z'/(h/L))$

a_{ij} deviatoric stress tensor

C_f local skin-friction coefficient $\left(= 2\tau_w/\rho U_\infty^2\right)$

C_p local pressure coefficient $\left(= 2(p - p_{\text{ref}})/\rho U_\infty^2\right)$

e_a approximate relative error of flow property for calculating GCI

e_{ext} extrapolated relative error of flow property for calculating GCI

H shape factor

h ramp height; also, grid size

h_d height of flat downstream section

h_u height of flat upstream section

k	turbulence kinetic energy
K_0	DARPA Suboff geometry constant
L	ramp length
L_z	distance between curved wall and top boundary
N	total number of cells used for computation; also, total number of grid points used for computation in wall normal direction N_z
n	wall normal direction
p	pressure (dynamic); also, apparent order
r	grid refinement factor
Re	Reynolds number ($= \rho UL/\mu$)
S_{ij}	strain-rate tensor
u	streamwise velocity
U_e	edge velocity
u_τ	friction velocity
x	Cartesian coordinate
z	Cartesian coordinate
z'	slope of ramp

ACKNOWLEDGMENTS

First of all, I would like to express sincere appreciation to my advisor, Professor Antonino Ferrante, for giving me the opportunity to engage in research in the Computational Fluid Mechanics group, for teaching me how to conduct research, for his guidance and encouragement as I worked on my thesis project.

Other professors that I would like to thank include Professor Owen Williams, for serving as the substitute member of my thesis committee when Professor Robert Breidenthal got sick, providing constructive comments and suggestions; Professor Robert Breidenthal, for reading the thesis and providing valuable comments; and Professor Dana Dabiri, for his guidance and suggestion in my first year.

I would like to thank Abhiram Aithal for his mentorship throughout this research project. His wisdom and diligence always inspires me to surpass myself.

Also, I want to thank David Fray for helping me to maximize the computational availability for my massive numerical simulations on Hyak.

I feel lucky to have a group of excellent and interesting friends in GUG 307, who always inspire and encourage me to think big, take challenge and be better.

Lastly, I thank my parents and parents-in-law for their support and for always believing in me. I would not finish my study without all they have sacrificed.

This work was facilitated though the use of advanced computational, storage, and networking infrastructure provided by the Hyak supercomputer system at the University of Washington.

DEDICATION

to my wife, Yaya, without whose endless love and support none of this would have been possible.

Chapter 1

INTRODUCTION

1.1 Motivation and Objectives

Flow separation is the detachment of the boundary layer from the surface of curved bodies due to the adverse pressure gradient. The study of flow separation remains a topic of considerable interest due to its frequent occurrence in practical flows. This phenomenon often appears in flows over airfoils, afterbodies of fuselage, and leads to increased aerodynamic drag. Moreover, in order to design low-drag aerodynamic geometries, we must be able to understand and predict the onset of flow separation and reattachment.

Reynolds-averaged Navier-Stokes (RANS) modeling is commonly used in the industry to design the aerodynamic geometries owing to its low computational cost. Presently, second-order finite-volume RANS solvers are widely used with meshes which may have more than 100 million cells (Witherden and Jameson [2017]). In spite of appreciable successes, the performance of RANS models in predicting turbulent-separated flows is unreliable (Slotnick et al. [2014]). However, the separation point is predicted reasonably well by most computational fluid dynamics (CFD) methods from RANS, large-eddy simulation (LES), blended RANS-LES to direct numerical simulation (DNS), while the reattachment point is predicted significantly downstream of the experimental location (Rumsey et al. [2004]).

Turbulence measurements around separation and reattachment is available for a turbulent boundary layer on a smooth, axisymmetric body exposed to an adverse pressure gradient. The sensitivity of boundary layers to small changes in pressure gradient near incipient separation is studied in Dengel and Fernholz [1990] and Alving and Fernholz [1996]. A small separation bubble is created using a tailored streamwise pressure gradient. It is shown that the skin friction drops sharply at the strongest adverse pressure gradient, and the separation actually occurs near a local minimum in the pressure gradient, and the flow reattaches in a mild adverse pressure gradient. In contrast, without imposing pressure gradient, an experimental study of a turbulent boundary layer separation over a

circular arc is presented by Song and Eaton [2004]. Several RANS and LES simulations have been recently performed for turbulent flow over curved wall (Fureby et al. [2015], Wasistho and Squires [2001, 2005], Radhakrishnan et al. [2006], El-Askary [2009], Bentaleb et al. [2012]). All of them are assessed by comparison with experimental measurement of Song and Eaton [2004]. In Wasistho and Squires [2001], the inflow boundary condition is obtained from a statistical two-dimensional turbulent boundary layer. Further, the differences in grids and boundary conditions represent an additional source of uncertainty when attempting to compare CFD results (Rumsey et al. [2004]).

Effects of surface curvature is reviewed in Patel and Sotiropoulos [1997] and Simpson [1989], convex and concave curvature is reported separately. In convex curvature region, then $\partial p/\partial n > 0$, and there is a reduction in entrainment downstream. Convex curvature reduces the momentum transport through a strong adverse pressure gradient turbulent boundary layer and causes separation to occur farther upstream. For concave curvature, $\partial p/\partial n < 0$ and greater entrainment, mixing and turbulent shearing stresses result.

In Hammache et al. [2002], digital particle image velocimetry (DPIV) measurement on an Stratford axisymmetric ramp is conducted. Two additional ramp shapes with shorter and longer ramp length corresponding to higher and lower adverse pressure gradient are tested for comparison with the original Stratford ramp along which the flow is incipient separation. However, it should be noted that the Stratford ramp has nearly constant slope, and zero curvature.

To the best of our knowledge there are no results in the literature regarding how a varying slope and curvature distribution of curved ramp affects the flow separation. In this thesis, we aim to answer the following question regarding flow separation over curved ramps:

- Can we find a way to predict flow separation by merely knowing few parameters related to the ramp geometry and the incoming flow?

To answer this question, we first establish a set of best-practices for setting up RANS simulations of turbulent flows over curved ramps. Next, we validated the RANS against experiments. Finally, we employ these guidelines to investigate the effects of the ramp geometry and inflow parameters, and establish a criterion for the incipient separation of turbulent flow over curved ramps based on the geometry and Reynolds number of the flow.

1.2 Flow separation

In this section, the process of flow separation is briefly discussed. Flow separation is referred to the flow reversal over a solid surface that occurs due to an adverse pressure gradient. The flow near the wall decelerates due to the adverse pressure gradient ($dp/dx > 0$) either prescribed at the boundary or induced by changing geometry. Figure 1.1(a) shows the typical velocity profiles undergoing different pressure gradients. Figure 1.1(b) illustrates the flow separation process. For steady, two-dimensional flow, vanishing of the surface shear stress or flow-reversal can be used as the criterion for separation. The location where flow starts to reverse is called incipient separation point ($\partial u/\partial y = 0$).

In flows studied in this thesis, the turbulent boundary layer separates due to the adverse pressure gradient induced by the curved walls.

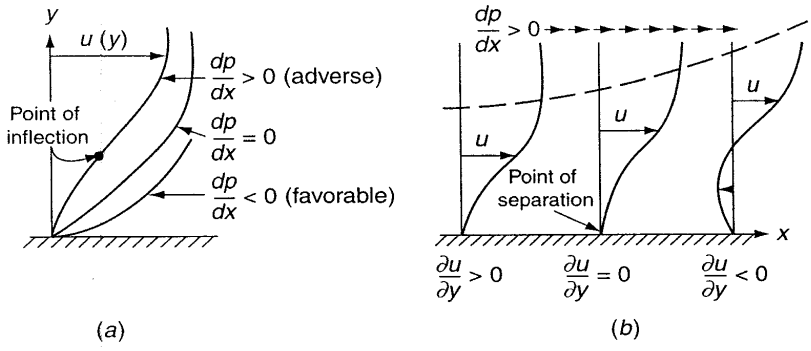

Figure 1.1: Sketch of flow separation process. (a) velocity profiles undergo different pressure gradients; (b) flow separation due to a persistent adverse pressure gradient. (White and Corfield [2006])

The thesis is organized as follows: Chapter 2 introduces the RANS turbulence modeling, the ANSYS Fluent flow solver, and the details of the flow configuration, generation of the computational grid, and boundary conditions. In Chapter 3, the performance of RANS modeling is assessed. Chapter 4 discusses the effects of ramp geometry and inflow conditions on the incidence of incipient separation and presents the criterion of incipient separation. Chapter 5 summarizes the findings and discusses potential future work.

Chapter 2

MATHEMATICAL MODELING

The governing equations for incompressible flows are

$$\nabla \cdot \mathbf{U} = 0, \tag{2.1}$$

$$\frac{\partial \mathbf{U}}{\partial t} + (\mathbf{U} \cdot \nabla)\mathbf{U} = -\frac{1}{\rho}\nabla p + \nu \nabla^2 \mathbf{U}, \tag{2.2}$$

where $\mathbf{U} = \mathbf{U}(\mathbf{x}, t)$ is the fluid velocity, $p = p(\mathbf{x}, t)$ is the pressure, ρ is the density, ν is the kinematic viscosity. An in-depth explanation of the theory of turbulent flows is given by Pope [2003].

2.1 Reynolds-averaged Navier-Stokes equations

The Reynolds decomposition of the instantaneous velocity, $\mathbf{U}(\mathbf{x}, t)$, into its mean, $\langle \mathbf{U} \rangle(\mathbf{x})$, and fluctuation, $\mathbf{u}(\mathbf{x}, t)$, is given by

$$\mathbf{U}(\mathbf{x}, t) = \langle \mathbf{U} \rangle(\mathbf{x}) + \mathbf{u}(\mathbf{x}, t), \tag{2.3}$$

where the brackets $\langle \ldots \rangle$ denote the spanwise and temporal averaging of the enclosed quantity. The velocity and pressure fields are decomposed into their mean and fluctuating components,

$$\mathbf{U} = \langle \mathbf{U} \rangle + \mathbf{u}, \quad p = \langle p \rangle + p', \tag{2.4}$$

where $\langle p \rangle$ and p' are mean and fluctuating pressure, respectively. The application of Reynolds decomposition results in the mean-continuity and mean-momentum or Reynolds equations

$$\frac{\partial}{\partial x_i} \langle U_i \rangle = 0, \tag{2.5}$$

$$\frac{\partial}{\partial t} \langle U_i \rangle + \langle U_j \rangle \frac{\partial}{\partial x_j} \langle U_i \rangle = -\frac{1}{\rho} \frac{\partial}{\partial x_i} \langle p \rangle + \frac{\partial}{\partial x_j} \left(2\nu \langle S_{ij} \rangle - \langle u_i u_j \rangle \right), \tag{2.6}$$

with the mean strain-rate tensor, $\langle S_{ij} \rangle$ defined as

$$\langle S_{ij} \rangle = \frac{1}{2} \left(\frac{\partial \langle U_i \rangle}{\partial x_j} + \frac{\partial \langle U_j \rangle}{\partial x_i} \right). \tag{2.7}$$

The Reynolds equations (Equation (2.6)) can be rewritten as

$$\frac{\partial}{\partial t}\left\langle U_i\right\rangle + \left\langle U_j\right\rangle \frac{\partial}{\partial x_j}\left\langle U_i\right\rangle = \frac{\partial}{\partial x_j}\left[-\frac{1}{\rho}\left\langle p\right\rangle \delta_{ij} + \nu\left(\frac{\partial\left\langle U_i\right\rangle}{\partial x_j} + \frac{\partial\left\langle U_j\right\rangle}{\partial x_i}\right) - \left\langle u_i u_j\right\rangle\right]. \tag{2.8}$$

The terms in square brackets represent three types of stresses (specific stress): the isotropic stress from mean pressure field, the viscous stress from momentum transfer at molecular level, and the stress from momentum transfer by the fluctuating velocity field, respectively. The additional term in Equation (2.8) $\left(-\frac{\partial}{\partial x_j}\left\langle u_i u_j\right\rangle\right)$ is called the Reynolds stress (and it is convenient to refer to $\left\langle u_i u_j\right\rangle$ as the Reynolds stress instead of specific Reynolds stress). The Reynolds stresses are the components of a symmetric second-order tensor. The diagonal components $\left(\left\langle u_1^2\right\rangle, \left\langle u_2^2\right\rangle, \text{and}\left\langle u_3^2\right\rangle\right)$ are normal stresses, while the off-diagonal components (e.g., $\left\langle u_1 u_2\right\rangle$) are shear stresses. The turbulence kinetic energy $k(\mathbf{x}, t)$ is defined as half of the trace of the Reynolds stress tensor

$$k \equiv \frac{1}{2}\left\langle \mathbf{u}\cdot\mathbf{u}\right\rangle = \frac{1}{2}\left\langle u_i u_i\right\rangle. \tag{2.9}$$

The Reynolds stress tensor can be decomposed into the isotropic stresses $(2/3k\delta_{ij})$ and the deviatoric stresses (a_{ij}) as

$$a_{ij} \equiv \left\langle u_i u_j\right\rangle - \frac{2}{3}k\delta_{ij}. \tag{2.10}$$

The Reynolds stress tensor has six independent elements as it is symmetric, thus there are six more unknowns in the Reynolds equations. This represents the closure problem of turbulence and the unclosed system of equations cannot be solved unless the Reynolds stresses are somehow determined.

2.2 Turbulent-viscosity hypothesis

The turbulent-viscosity hypothesis was introduced by Boussinesq, and is mathematically analogous to the stress-rate-of-strain relation for a Newtonian fluid shown below

$$\tau_{ij} = -P\delta_{ij} + \mu\left(\frac{\partial U_i}{\partial x_j} + \frac{\partial U_j}{\partial x_i}\right). \tag{2.11}$$

According to the hypothesis, the deviatoric Reynolds stress (a_{ij}) is proportional to the mean rate of strain, then

$$-\rho a_{ij} = \rho\nu_t\left(\frac{\partial\left\langle U_i\right\rangle}{\partial x_j} + \frac{\partial\left\langle U_j\right\rangle}{\partial x_i}\right) = 2\rho\nu_t\left\langle S_{ij}\right\rangle \tag{2.12}$$

where the positive scalar coefficient ν_t is the turbulent or eddy viscosity. We obtain the following modified mean-momentum equation by introducing the turbulent-viscosity hypothesis

$$\frac{\partial}{\partial t}\langle U_i\rangle + \langle U_j\rangle \frac{\partial}{\partial x_j}\langle U_i\rangle = \frac{\partial}{\partial x_j}\left[\nu_{\text{eff}}\left(\frac{\partial\langle U_i\rangle}{\partial x_j} + \frac{\partial\langle U_j\rangle}{\partial x_i}\right)\right] - \frac{1}{\rho}\frac{\partial}{\partial x_i}\left(\langle p\rangle + \frac{2}{3}\rho k\right), \tag{2.13}$$

where

$$\nu_{\text{eff}}(\mathbf{x}, t) = \nu + \nu_t(\mathbf{x}, t) \tag{2.14}$$

is the effective viscosity. Equation (2.13) is the same as the incompressible Navier-Stokes equation with $\langle\mathbf{U}\rangle$, ν_{eff} and the modified mean pressure $(\langle p\rangle + 2/3\rho k)$ in place of $\mathbf{U}$, ν and p respectively. The next step is to model ν_t.

2.3 Spalart-Allmaras model

2.3.1 Overview

The Spalart-Allmaras model (Spalart and Allmaras [1992]) is a one-equation model that solves a modeled transport equation for the kinematic turbulent viscosity. The Spalart-Allmaras model was designed specifically for aerospace applications involving wall-bounded flows and has been shown to give good results for boundary layers subjected to adverse pressure gradients (ANSYS Inc).

2.3.2 Transport equation for the Spalart-Allmaras model

The transported variable in the Spalart-Allmaras model, $\tilde{\nu}$, called modified turbulent viscosity, is identical to the turbulent kinematic viscosity, ν_t, except in the near-wall (viscosity-affected) region. The transport equation for $\tilde{\nu}$ used to form the kinematic eddy viscosity is written as

$$\frac{\partial\tilde{\nu}}{\partial x} + \langle U_j\rangle \frac{\partial\tilde{\nu}}{\partial x_j} = G_v - Y_v + \frac{1}{\sigma}\left[\frac{\partial}{\partial x_j}\left((\nu + \tilde{\nu})\frac{\partial\tilde{\nu}}{\partial x_j}\right) + c_{b2}\frac{\partial\tilde{\nu}}{\partial x_i}\frac{\partial\tilde{\nu}}{\partial x_i}\right], \tag{2.15}$$

where G_v is the production of turbulent viscosity, and Y_v is the destruction of turbulent viscosity that occurs in the near-wall region due to wall blocking and viscous damping. The kinematic eddy viscosity is expressed in terms of modified kinematic turbulent viscosity, also called the working variable of the turbulence model as

$$\nu_t = \tilde{\nu} f_{v1}, \quad f_{v1} = \frac{\chi^3}{\chi^3 + c_{v1}^3}, \quad \chi \equiv \frac{\tilde{\nu}}{\nu}, \tag{2.16}$$

where f_{v1} is the viscous damping function. The production term, G_v, is modeled as

$$G_v = c_{b1}\tilde{S}\tilde{\nu}, \quad \tilde{S} \equiv S + \frac{\tilde{\nu}}{\kappa^2 d^2} f_{v2}, \quad f_{v2} = 1 - \frac{\chi}{1 + \chi f_{v1}}, \tag{2.17}$$

where d is the distance from the wall, and S is a scalar measure of the deformation tensor, which is based on the magnitude of the vorticity:

$$S \equiv \sqrt{2\Omega_{ij}\Omega_{ij}}, \tag{2.18}$$

where Ω_{ij} is the mean rate-of-rotation tensor and is defined by

$$\Omega_{ij} = \frac{1}{2}\left(\frac{\partial \langle U_i \rangle}{\partial x_j} - \frac{\partial \langle U_j \rangle}{\partial x_i}\right). \tag{2.19}$$

The destruction term is modeled as

$$Y_v = c_{w1} f_w \left(\frac{\tilde{\nu}}{d}\right)^2, \tag{2.20}$$

where the blending function f_w is

$$f_w = g\left[\frac{1 + c_{w3}^6}{g^6 + c_{w3}^6}\right]^{1/6}, \quad g = r + c_{w2}(r^6 - r), \quad r \equiv \frac{\tilde{\nu}}{\tilde{S}\kappa^2 d^2}. \tag{2.21}$$

The eight model closure coefficients are:

$$c_{b1} = 0.1355, \quad c_{b2} = 0.622, \quad c_{v1} = 7.1, \quad \sigma = 2/3$$
$$c_{w1} = \frac{c_{b1}}{\kappa^2} + \frac{1 + c_{b2}}{\sigma}, \quad c_{w2} = 0.3, \quad c_{w3} = 2.0, \quad \kappa = 0.4187$$

2.4 Numerical solution procedure

2.4.1 Introduction of flow solver

The numerical simulations are carried out using the computational fluid dynamics software called ANSYS Fluent. ANSYS Fluent is a commercial flow solver using the finite volume method (FVM), which solves the integral form of governing equations for the conservation of mass, momentum, and other scalars qualities. The computational domain is divided into a finite number of small control volumes (CVs) using a grid which defines the control volume edges. On each individual CV, the governing equations of discrete dependent variables such as velocities, pressure, and conserved scalars are integrated to construct a system of algebraic equations. The nonlinear algebraic equations are then linearized, and the resultant linear equation system is solved iteratively to yield updated values of the dependent variables when errors are smaller than a specific tolerance.

2.4.2 Solver theory

ANSYS Fluent solves the discretized equations in a pressure-based segregated method, using SIMPLE and PISO algorithms. Both algorithms belong to a general class of methods called the projection method. In this method, the constrain of continuity of the velocity field is achieved by solving a pressure equation. The pressure equation is derived from the continuity and the momentum equations in such a way that the velocity field, corrected by the pressure, satisfies the continuity equation. Since the governing equations are nonlinear and coupled, the solution process involves iterations wherein the entire set of governing equations is solved repeatedly until the solution converges. Each iteration step is illustrated in Figure 2.1.

2.4.3 Procedure of test case setup and calculation

All ANSYS Fluent settings are included in a journal file (see Appendix B). The procedure of test case setup is illustrated in Figure 2.2.

2.5 Flow configuration

2.5.1 Computational domain

The schematic of computational domain is shown in Figure 2.3. The wall is composed of two flat sections (upstream, $x/L < 0$, and downstream, $x/L > 1$) and a curved ramp, $0 \leq x/L \leq 1$ whose definitions are provided in § 4.1.1. The original ramp geometry (NASA1) used for RANS assessment cases is a fifth-order polynomial introduced by Disotell and Rumsey [2017]. The ramp height, h, is defined as the height difference between upstream and downstream flat sections. All geometrical length scales are non-dimensionalized by the ramp length, L. The steepest ramp, over which the adverse pressure gradient is highest of all test cases, has $h/L = 0.4$. The flow domain dimensions and inflow parameters of RANS assessment cases are shown in Table 2.1.

2.5.2 Boundary conditions

The following boundary conditions are applied in all RANS simulations.

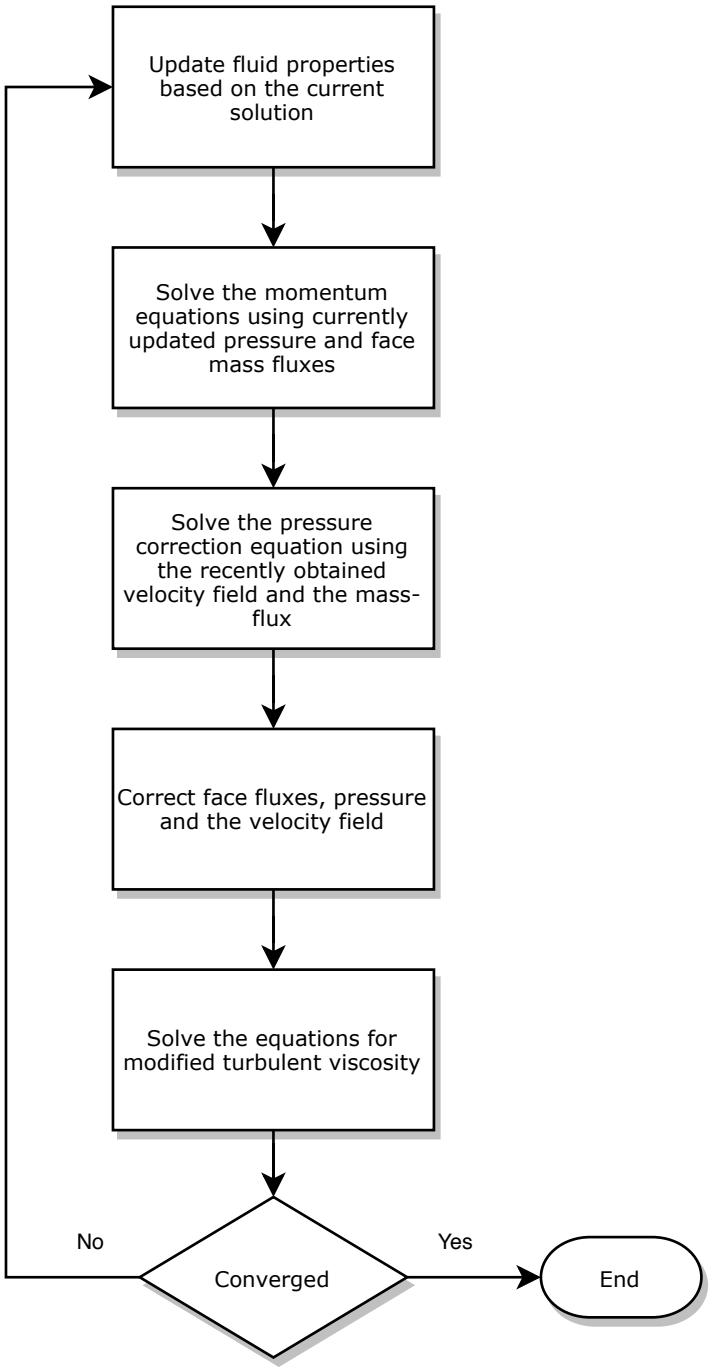

Figure 2.1: Overview of pressure-based segregated method.

Test case setup

- Import grid
- Scale grid
- Define viscous model:
  - Spalart-Allmaras
- Define material properties
- Define boundary
- Interpret user defined function (UDF)
- Import velocity profile
- Define boundary conditions
- Define solver
  - Scheme: SIMPLE
  - Gradient: Least Squares Cell Based
  - Pressure: Second Order
  - Momentum: Second Order Upwind
  - Modified Turbulent Viscosity: Second Order Upwind
- Define residual
  - 1e-06

Calculation

- Initialization
- Save case file
- Solve steady-state iterations
- Save case and data file as initial condition for transient iterations
- Define solver
  - Scheme: PISO
  - Gradient: Least Squares Cell Based
  - Pressure: Second Order
  - Momentum: Second Order Upwind
  - Modified Turbulent Viscosity: Second Order Upwind
- Define time step
  - Time step interval: 1e-05
  - Number of time step: 20000
  - Number of iterations in each time step: 200
- Solve transient iterations
- Save case and data file
- Post process

Figure 2.2: Procedure of test case setup and calculation.

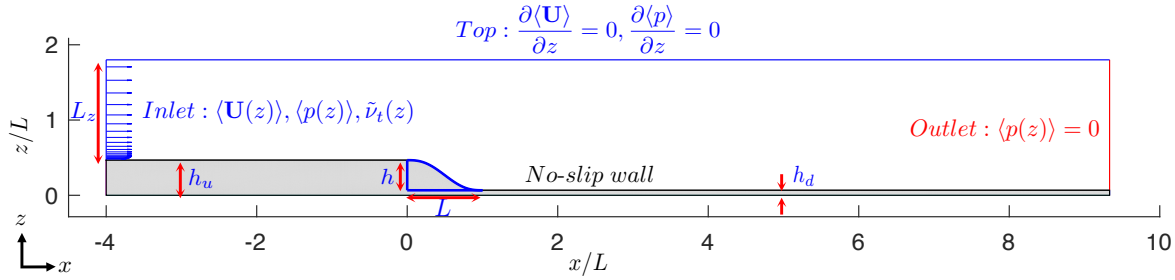

Figure 2.3: Schematic of the flow domain and boundary conditions. The dimensions scaled by the ramp length L. The original ramp geometry (NASA1) used for RANS assessment cases is formulated by a fifth-order polynomial introduced by § 4.1.1.

$L\ (m)$	h	δ_i	$L_{z,i}$	$L_{z,o}$	$U_\infty\ (m/s)$	Re_L	$Re_{\delta,i}$	$Re_{\theta,i}$	$Re_{\delta^*,i}$
0.25	$0.4L$	$L/25$	$33.3\delta_i$	$43.3\delta_i$	11.7	2×10^5	$8,000$	983	1456

Table 2.1: Flow domain dimensions and inflow parameters of RANS assessment cases.

Inlet

A velocity profile is prescribed at the inflow plane. In § 3.2.2, three different inflow velocity profiles are evaluated: uniform velocity profile, velocity profile according to the Blasius solution, and a mean velocity profile obtained by a flat-plate turbulent boundary layer simulation. All three profiles have the same free stream velocity magnitude, U_∞, and inflow boundary layer thickness δ_i. The Reynolds number is $Re_L = 2 \times 10^5$. In § 4.2, flows with different free stream velocities and inflow boundary layer thicknesses are investigated.

Outlet

At the outflow plane, the pressure outlet boundary condition is used. This involves extrapolation of the flow properties from the interior of the domain. In ANSYS Fluent, a specification of the static pressure at the pressure outlet is also needed and the default value of gauge pressure of zero is used.

Top (Far field)

The Neumann condition of zero velocity gradient is imposed at the far-field boundary of the domain. The free shear boundary condition is implemented by using a user defined function (UDF) since this boundary condition is not a built-in option in ANSYS Fluent. The velocity inlet boundary condition is selected at the top in order to apply UDF to both velocity components. The pressure at top is adjusted by ANSYS Fluent itself so as to satisfy the prescribed zero velocity gradient.

Wall

The no-slip boundary condition is imposed at the wall boundary.

2.6 Grid generation

The structured grid employed in all the simulations is composed of three blocks corresponding to three sections of the flow domain. A portion of the whole solution domain is shown in Figure 2.4.

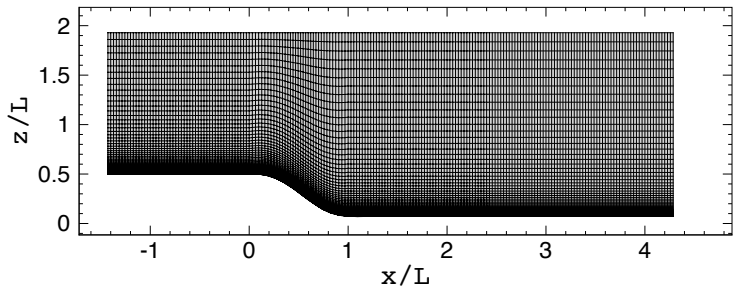

Figure 2.4: Portion of reduced numerical grid (near ramp section): only every fourth grid line is shown. Dimensions scaled by the ramp length. The onset of ramp locates at $x/L = 0$.

In the flat upstream and downstream sections, the grid spacing is uniform in streamwise direction (x), and stretched in the wall-normal direction (z) according to the wall stretching function used in Ferrante and Elghobashi [2004],

$$z = L_z \left[1 - \frac{tanh\gamma(L_z - \zeta)}{tanh\gamma L_z} \right] \tag{2.22}$$

N_z	z_i^+	z_o^+	γ_i	γ_o
128	0.13	0.11	0.44	0.35
192	0.09	0.07	0.44	0.35
255	0.06	0.06	0.44	0.35

Table 2.2: Grid property of RANS assessment cases ($U_\infty = 11.7$, $\delta_i = L/25$, $Re_L = 2 \times 10^5$).

where γ is stretching factor which determines the degree of grid stretching, and L_z is defined as the local height from wall to far field boundary. It is worth noting that L_z affects the degree of grid compression in addition to γ.

In the ramp section, however, L_z increases continuously from the onset of the ramp to the end. Therefore, given the same γ, the grid in ramp and the flat downstream sections is compressed more than the flat upstream section. Therefore, appropriate values of γ are determined in order to meet z^+ requirement of the closest grid point to the wall. Also, the streamwise discretization of ramp is achieved by using constant arc length rather than uniform streamwise grid spacing. This avoids any undesired grid clustering at regions of high ramp slope.

The superscript + represents a quantity expressed in wall-units: $\langle U \rangle^+ = \langle U \rangle / u_\tau$, $\langle uv \rangle^+ = \langle uv \rangle / u_\tau^2$ and $z^+ = z u_\tau / \nu$ where the friction velocity $u_\tau = \sqrt{\tau_w / \rho}$ and τ_w is the wall shear stress.

In this simulations, the near-wall region of the boundary layer is fully resolved by maintaining the z^+ of wall-adjacent cell to be less than 1. The closest grid point for all cases is located at $z^+_{\max} < 0.4$. Therefore, the level of grid resolution employed here allows us to circumvent the need for using wall functions in the near-wall region.

The grid stretching factors used for RANS assessment cases are shown in Table 2.2. In the ramp section, γ is obtained by interpolation between the upstream stretching factor γ_i and the downstream γ_o. The wall-adjacent cell height $z^+_{\min}$ along the ramp is plotted in Figure 2.5.

The stretched grid (z) is generated by mapping from a uniform grid (ζ) by using Equation (2.22). The grid coordinates are written in Plot3d format and imported into ANSYS Fluent. The four domain boundaries are then separated to form the external boundaries.

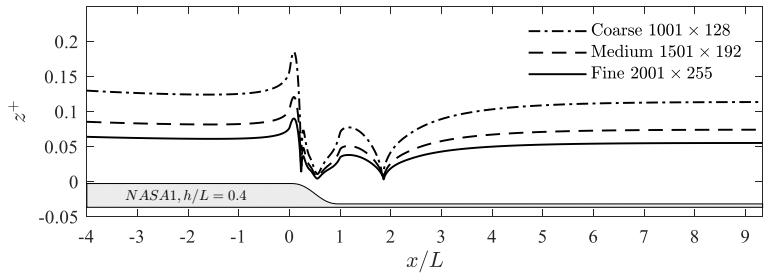

(a)

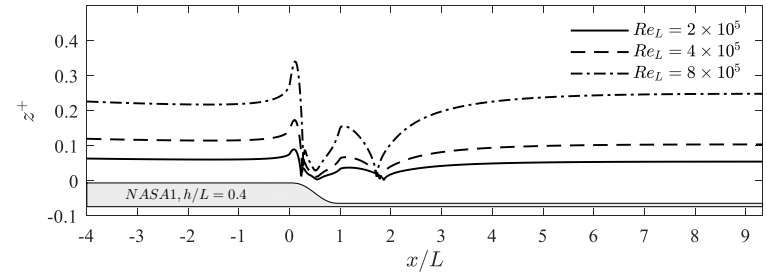

(b)

Figure 2.5: z^+ distribution along the wall. (a) three grid resolutions; (b) three Reynolds numbers.

Chapter 3

RANS MODEL ASSESSMENT

The performance of Spalart-Allmaras RANS model in simulating turbulent boundary layer flows with separation is assessed in this chapter. Further, the guidelines to setup a RANS simulation of this kind have been investigated. The following three components of the simulation setup are examined: 1) computational grid; 2) inflow boundary condition; 3) computational domain size. Based on our investigations, we establish a set of best-practices for setting up RANS simulations. We also validate the flow solver by comparing the results with published experiments for flow over a curved ramp (Song and Eaton [2004]). All RANS assessment cases are tabulated in Table 3.1.

3.1 Grid convergence study

The grid convergence study is carried out on meshes of 1001×128 (course), 1501×192 (medium), and 2001×255 (fine) grid points (cases A1, A2 and A3 respectively). Figure 3.1 shows the pressure and skin friction coefficient as a function of streamwise location for the three meshes. In order to provide a quantitative measure of the grid convergence, the grid convergence index (GCI) approach devised by Roache [1994] is adopted in this study. The recommended procedure for estimation of discretization error is given by Celik et al. [2008].

3.1.1 Grid convergence index (GCI)

For a given flow property ϕ, let ϕ_1, ϕ_2, and ϕ_3 be the solutions on a fine grid, a medium grid, and a coarse grid, respectively. The grid size h for a given grid is defined as

$$h = \left[\frac{1}{N} \sum_{i=1}^{N} (\Delta A_i) \right]^{1/2}, \tag{3.1}$$

where ΔA_i is the area of the ith cell, and N is the total number of cells in the mesh.

According to the recommended procedure in Celik et al. [2008], the grid refinement factor $r = h_{\text{coarse}}/h_{\text{fine}}$ should to be greater than 1.3. In this study, $r_{21} = h_2/h_1 = 1.33$, $r_{32} = h_3/h_2 = 1.50$.

Case	N_z	Inlet B/C	δ_i/L	Domain*	Geometry**	h/L
A1	128	Turbulent	1/25	L U/S + L D/S	NASA1	0.4
A2	192	Turbulent	1/25	L U/S + L D/S	NASA1	0.4
A3	255	Turbulent	1/25	L U/S + L D/S	NASA1	0.4
B1	255	Turbulent	1/25	L U/S + L D/S	NASA1	0.4
B2	255	Turbulent	1/25	S U/S + S D/S	NASA1	0.4
C1	255	Uniform	1/25	L U/S + L D/S	NASA1	0.4
C2	255	Blasius	1/25	L U/S + L D/S	NASA1	0.4
C3	255	Turbulent	1/25	L U/S + L D/S	NASA1	0.4
C4	255	Uniform	1/25	L U/S + S D/S	NASA1	0.4
C5	255	Blasius	1/25	L U/S + S D/S	NASA1	0.4
C6	255	Turbulent	1/25	L U/S + S D/S	NASA1	0.4
C7	255	Uniform	1/25	S U/S + L D/S	NASA1	0.4
C8	255	Blasius	1/25	S U/S + L D/S	NASA1	0.4
C9	255	Turbulent	1/25	S U/S + L D/S	NASA1	0.4
C10	255	Uniform	1/25	S U/S + S D/S	NASA1	0.4
C11	255	Blasius	1/25	S U/S + S D/S	NASA1	0.4
C12	255	Turbulent	1/25	S U/S + S D/S	NASA1	0.4

* Domain is composed of ramp and different lengths (long and short) of the upstream and downstream sections.

** NASA1 is formulated by a fifth-order polynomial provided in Table 4.1.

Table 3.1: Simulation matrix of RANS model assessment

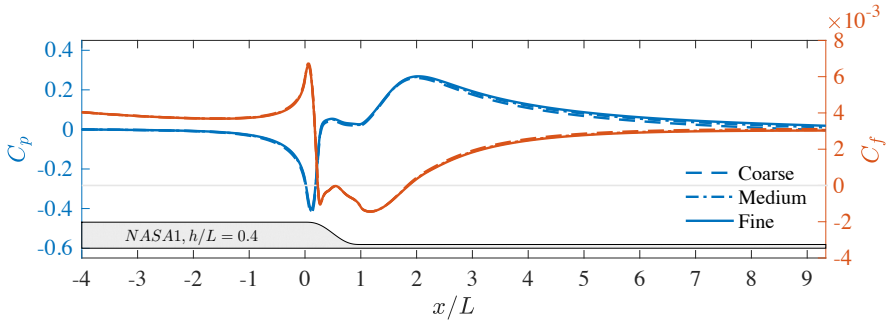

Figure 3.1: Pressure coefficient, C_p, and skin friction coefficient, C_f, distribution along curved wall. (Geometry: NASA1, $h/L = 0.4$; dashed line, course grid $N_z = 128$; dashed-dot line, medium grid $N_z = 192$; solid line, fine grid $N_z = 255$; gray line, $C_f = 0$.)

The errors between three different grids are given as $\epsilon_{32} = \phi_3 - \phi_2$, $\epsilon_{21} = \phi_2 - \phi_1$. The apparent order p of the GCI method can be calculated by using following expressions

$$p = \frac{1}{\ln(r_{21})} \left| \ln \left| \frac{\epsilon_{32}}{\epsilon_{21}} \right| + q(p) \right|, \tag{3.2a}$$

$$q(p) = \ln \left(\frac{r_{21}^p - s}{r_{32}^p - s} \right), \tag{3.2b}$$

$$s = 1 \cdot \operatorname{sgn} \left(\frac{\epsilon_{32}}{\epsilon_{21}} \right). \tag{3.2c}$$

Equations 3.2 can be solved for p using the fixed-point iteration method. The extrapolated values are then calculated as

$$\phi_{\text{ext}}^{21} = \frac{r_{21}^p \phi_1 - \phi_2}{r_{21}^p - 1}. \tag{3.3}$$

Finally, the fine-grid convergence index is calculated as

$$GCI_{\text{fine}}^{21} = \frac{1.25 e_a^{21}}{r_{21}^p - 1}, \tag{3.4}$$

where approximate relative error is given by

$$e_a^{21} = \left| \frac{\phi_1 - \phi_2}{\phi_1} \right|, \tag{3.5}$$

and the extrapolated relative error is given by

$$e_{\text{ext}}^{21} = \left| \frac{\phi_{\text{ext}}^{21} - \phi_1}{\phi_{\text{ext}}^{21}} \right|. \tag{3.6}$$

Variable	p	e_a^{21}	e_{ext}^{21}	GCI_{fine}^{21}
$C_{f,x/L=-0.2}$	2.2073	0.55%	0.63%	0.78%
$C_{p,x/L=-0.2}$	2.0940	3.03%	3.84%	4.62%
$C_{f,x/L=0}$	1.9552	0.60%	0.81%	1.00%
$C_{p,x/L=0}$	2.2193	2.24%	2.59%	3.16%
$C_{f,x/L=1.5}$	1.1292	0.57%	1.47%	1.87%
$C_{p,x/L=1.5}$	2.0022	1.00%	1.27%	1.61%
x_{separate}/L	1.6088	0.30%	0.51%	0.64%
x_{reattach}/L	2.1245	0.43%	0.51%	0.64%

Table 3.2: Calculation of discretization error

The GCI for skin friction coefficient at $x/L = -0.2,\ 0,\ 1.5$, pressure coefficient at $x/L = -0.2,\ 0,\ 1.5$, and separation and reattachment lengths of the flow over the steepest ramp ($h/L = 0.4$) are shown in Table 3.2. The overall GCI of all the above tabulated quantities are under 5%.

3.2 Inflow conditions

In this section, three different velocity profiles are discussed in detail: 1) the uniform velocity profile used in Disotell and Rumsey [2017]; 2) the turbulent velocity profile used in Wasistho and Squires [2005]; 3) Blasius velocity profile. The goal is to find the most suitable velocity boundary condition for RANS simulations of flow over curved ramps.

3.2.1 Turbulence parameter setup

For Spalart-Allmaras model, turbulent viscosity ratio (TVR), the ratio of turbulent viscosity to molecular viscosity, needs to be specified at every boundary. In Spalart and Rumsey [2007], the recommended free stream turbulent parameter is $\chi = \tilde{\nu}/\nu = 3$. Next, the corresponding TVR is calculated as:

$$\frac{\mu_t}{\mu} = \frac{\nu_t}{\nu} = 0.21044. \tag{3.7}$$

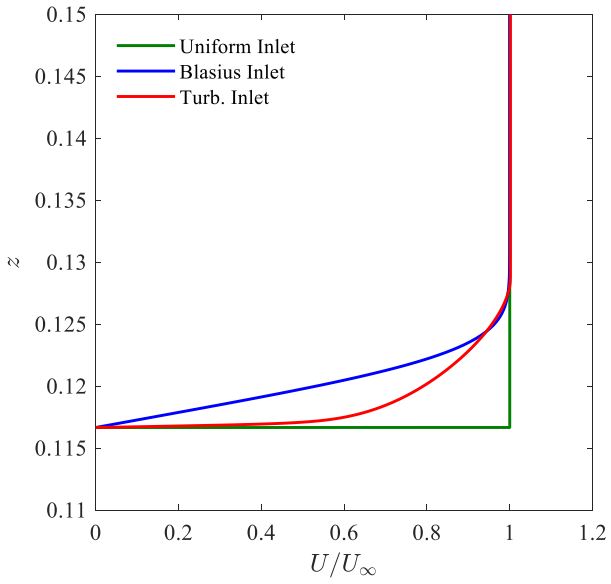

Figure 3.2: Inlet velocity profiles with the same U_∞ and $\delta_i = L/25$.

This value is used at all boundaries except at the wall, where $\nu_{t,w} = 0$.

3.2.2 Inflow velocity profiles

The three inflow velocity profiles are plotted in Figure 3.2. The boundary layer thickness of the Blasius and the mean turbulent profile are equal.

Turbulent inlet profile

The turbulent velocity profile is extracted from a precalculated flat plate turbulent boundary layer simulation which has the same grid properties and parameter setup. To validate the turbulent inflow boundary condition, the mean streamwise velocity and Reynolds stress profile at $Re_\theta = 1430$ is extracted and compared with the experimental (De Graaff and Eaton [2000]) and DNS data (Ferrante and Elghobashi [2004]) in Figure 3.3.

It is seen from Figure 3.3(a) that the mean streamwise velocity is in good agreement with the experimental and DNS data while the RANS solution has a slight overshoot of about 2% from

the free stream velocity. Good agreement of the RANS with the DNS results is also obtained for the Reynolds shear stress $\langle uv \rangle$. The difference in the magnitude of the peak of $\langle uv \rangle$ is likely due to experimental uncertainty as stated in Ferrante and Elghobashi [2004]. Therefore, the mean velocity profiles at desired boundary layer thickness can then be extracted at different locations. In ANSYS Fluent, the mean profiles are written into a *.prof* file, which includes mean pressure, mean streamwise velocity, mean transverse velocity, and the modified turbulent viscosity. Figure 3.4 shows an example of the mean profile in wall unit which has a boundary layer thickness of $\delta_i = L/25$ at three Reynolds numbers $Re_L = 2 \times 10^5,\ 4 \times 10^5,\ 8 \times 10^5$.

3.3 Computational domain

The dimensions of the computational domain in cases B1 and B2 are long and short respectively. Figure 3.5 shows the streamwise distribution of C_f and C_p for the two domain sizes. The discrepancy in the two curves are clearly seen in: 1) the region approaching the onset of ramp; 2) flow reattachment and downstream region. The long upstream section allows the boundary layer to develop under zero pressure gradient and then experience the pressure gradient induced by ramp. This can be also observed in the decrease of C_f at the beginning of long upstream region. However, the region of constant C_p is not found in the short upstream cases. The adverse pressure gradient induced by ramp affects the upstream region of the flow so that, for short domain, the prescribed inflow boundary condition is subject to unphysical adjustment. Therefore, the upstream length is a crucial parameter in the setup of the simulation. Also, the outlet is a pressure boundary condition with zero gauge pressure. A longer downstream allows flow to fully recover, and for the pressure gradient to approach close to zero.

3.4 Effects of inflow boundary conditions

3.4.1 Effect of velocity profile on flow development in the upstream section

Figure 3.6 shows the streamwise development of skin friction coefficient and coefficient of pressure for different inflow velocity profiles.

The C_f in the upstream section is disparate due to the velocity gradient at the wall, $(\partial u/\partial z)_w$. For a uniform velocity, the discontinuity at the wall leads to a large value of C_f. Also, larger velocity

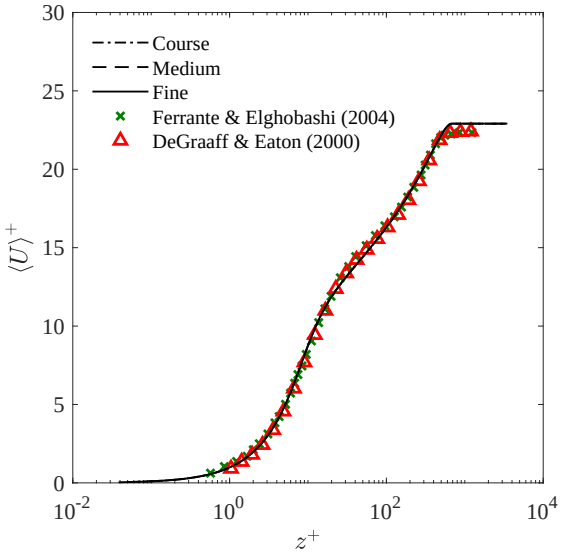

(a) Mean streamwise velocity

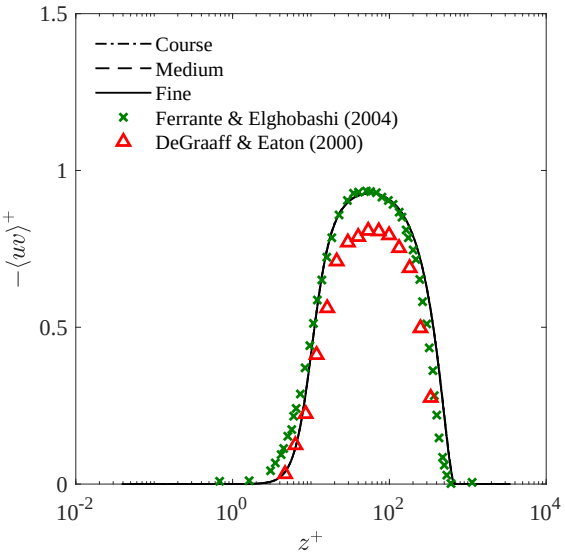

(b) Reynolds stress

Figure 3.3: Mean streamwise velocity profile and Reynolds stress at $Re_\theta = 1430$. Present RANS Spalart-Allmaras model, (dashed-dot line, course grid $N_z = 128$; dashed line, medium grid $N_z = 192$; solid line, fine grid $N_z = 255$).

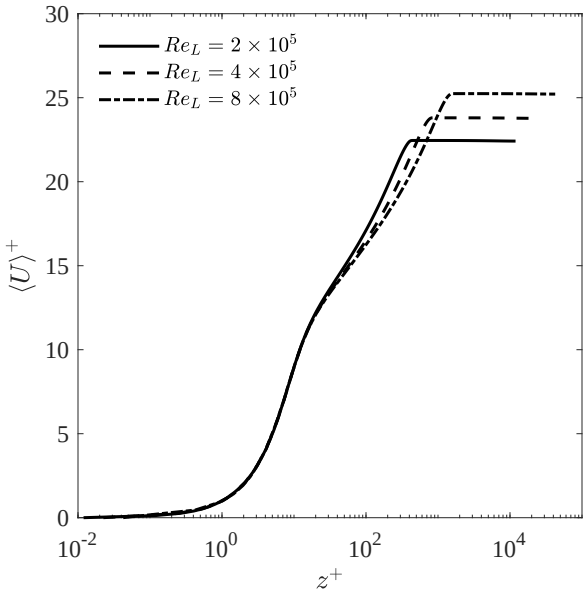

Figure 3.4: Mean streamwise velocity profile with $\delta_i = L/25$ at three Reynolds number. (dashed-dot line, $Re_L = 8 \times 10^5$; dashed line, $Re_L = 4 \times 10^5$; solid line, $Re_L = 2 \times 10^5$).

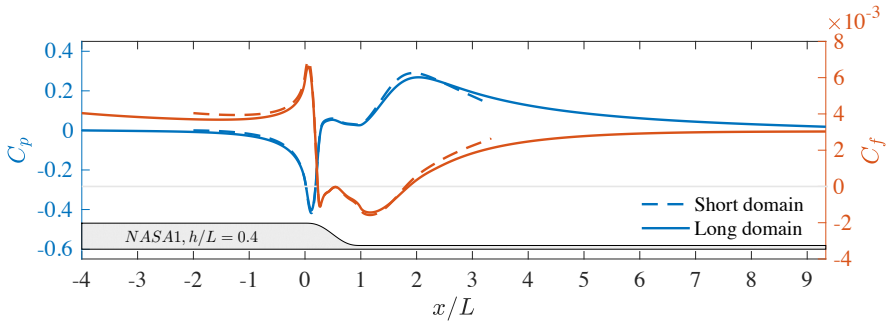

Figure 3.5: Pressure coefficient and skin friction coefficient distribution along the curved wall. The reference pressure is located at inlet. (dashed line, short domain; solid line, long domain)

gradient of turbulent velocity profile gives higher C_f than the one of the Blasius inflow. Similar behavior can also be observed for C_p.

3.4.2 Effect of domain size

The effect of the domain size is clearly evident in Figures 3.6(a) and 3.6(c). First, the peak C_f at the onset of the ramp ($x/L = 0$) is different for Blasius and turbulent inflow conditions. Similar behavior can be observed for the local minimum of C_p at $x/L \approx 0$ in Figures 3.7(a) and 3.7(c).

However, no obvious difference can be seen in the behavior of C_f in Figures 3.6(a) and 3.6(b) or of C_p in Figures 3.7(a) and 3.7(b). Therefore, the downstream length does not affect the C_f and C_p distributions as much as the upstream length. For the cases with long upstream, Blasius and turbulent inflow profiles give similar C_f and C_p distribution over the ramp section.

3.4.3 Effect of velocity profile on flow development in the ramp section

Figure 3.8 shows the streamwise distribution of C_f and C_p over the ramp section. The following observations can be made from Figure 3.8,

1. C_f and C_p distribution in the ramp section for three velocity profiles show similar behavior. However, there is clear difference in the local minimum values of C_f and C_p for the uniform velocity inlet case.

2. The uniform velocity inlet case is more sensitive to the upstream length than when turbulent velocity inflow condition is used. This is due to the fact that the turbulent inflow profile is extracted from a well developed flat plate turbulent boundary layer flow in contrast to the uniform free stream velocity profile. Further, the boundary layer thickness in the case of turbulent velocity inlet does not increase as much as that of the uniform inlet profile case. Therefore, there is a large difference in peak C_f at upstream section.

3. In the case of Blasius inlet, C_f of longer upstream length is larger than that of short upstream length, which disagrees with the C_f of a developing boundary layer. Therefore, it implies that the boundary layer development for Blasius inlet profile has an unphysical adjustment, especially for short upstream domain.

$Re_{\theta,\text{ref}}$	$U_{e,\text{ref}}$ (m/s)	δ_{99} (mm)	Temp (K)	Pressure (Pa)	$\nu \times 10^6$ (m^2/s)
1,100	6.52	25.6	293.0	101,300	15.1

Table 3.3: Flow conditions of test case. The reference station is defined at $x/L = -2$.

Thus, we conclude that, the turbulent velocity profile is the proper way to prescribe the inlet boundary condition.

3.5 Validation

In this section, a comparison with experimental measurements (Song and Eaton [2004]) for turbulent flow over a contoured ramp is provided using two meshes of sizes 1501×192. The ramp geometry is a segment of a circular arc and the flow schematic is shown in Figure 3.9.

The simulation parameters are given in Table 3.3.

Based on the analysis in § 3.4, a turbulent inlet profile with longer upstream length is desired for RANS simulations. Therefore, in this validation case, the flow domain is extended two ramp lengths further upstream (at $x/L = -4$) to ensure that inflow boundary conditions are not subjected to the downstream pressure gradient. A turbulent inflow velocity profile is extracted from a turbulent flat plat boundary layer solution and prescribed at the inlet boundary so that the boundary layer thickness at $x/L = -2$ matches that of the experimental measurements.

Figure 3.10 shows the static pressure coefficient, $C_p = 2(p - p_{x/L=-1.81})/\rho U_{\text{ref}}^2$, along the wall. In order to match the boundary condition, the top boundary condition is set to be no-slip wall, and the grid is stretched towards both top and bottom wall. A favorable pressure gradient approaching the ramp ($-2 \leq x/L \leq 0$) due to streamline curvature over the ramp is well captured by present RANS simulation. The minimum C_p is underestimated which can be seen in LES result as well. A strong adverse pressure gradient is seen up to nearly two ramp lengths.

Figure 3.11 shows the comparison of skin friction coefficient, $C_f = 2\tau_w/\rho U_{\text{ref}}^2$, along the wall. The grid resolution is identical to the ones used for RANS assessment simulations. In the favorable pressure gradient region, the boundary layer becomes thinner which leads to the increase of C_f up

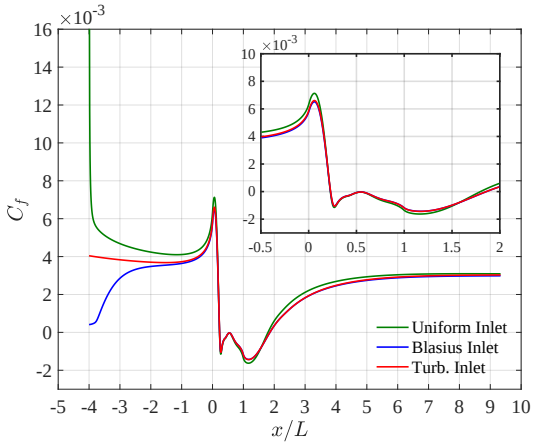

(a) Long upstream and long downstream

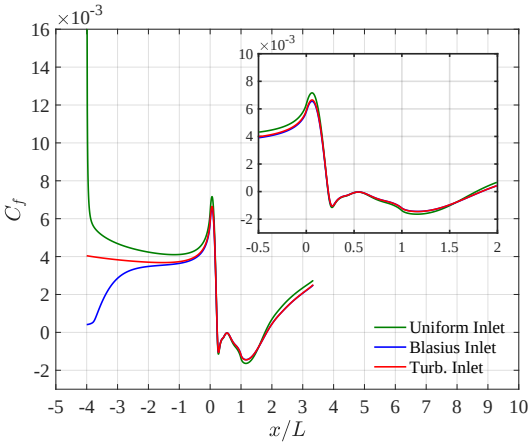

(b) Long upstream and short downstream

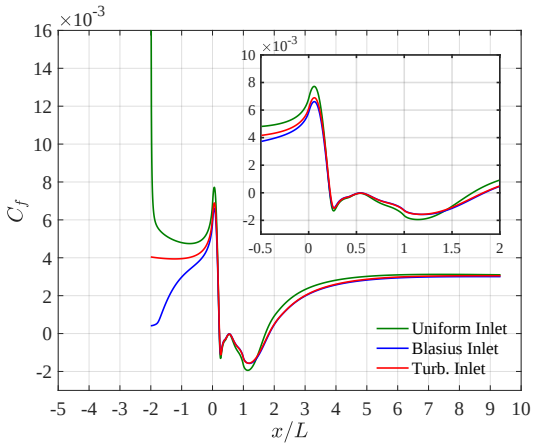

(c) Short upstream and long downstream

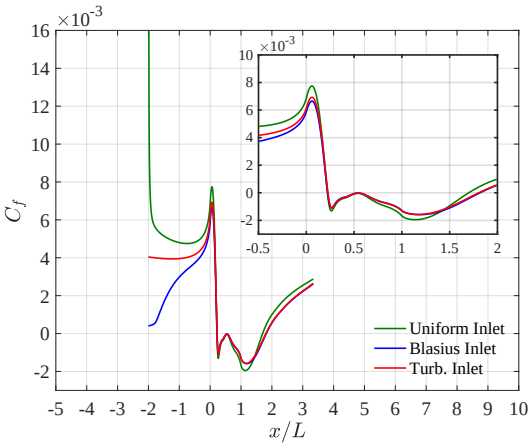

(d) Short upstream and short downstream

Figure 3.6: Skin friction coefficient distribution along the curved wall (NASA1, $h/L = 0.4$). The computational domain has a common ramp section and various length of upstream and downstream sections. Also, three different velocity profile has prescribed at inflow plane. The distribution near ramp section is shown in zoom in plot.

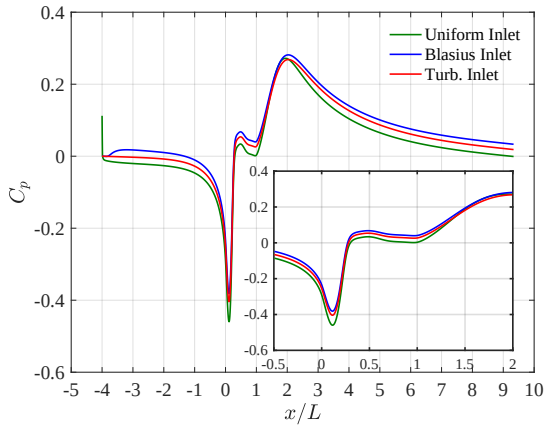

(a) Long upstream and long downstream

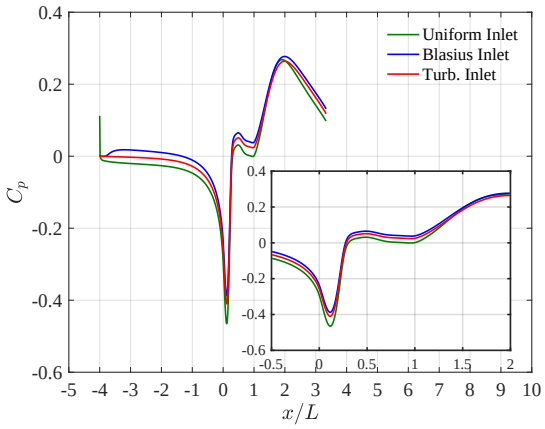

(b) Long upstream and short downstream

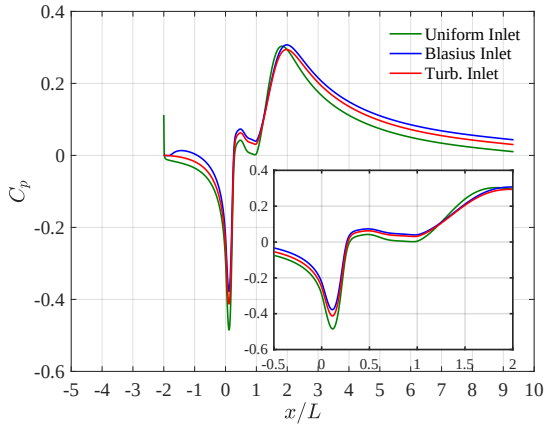

(c) Short upstream and long downstream

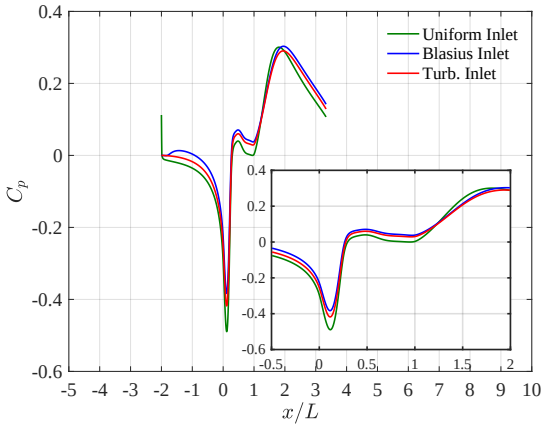

(d) Short upstream and short downstream

Figure 3.7: Pressure coefficient distribution along the curved wall (NASA1, $h/L = 0.4$). The reference station is defined at inlet. The computational domain has a common ramp section and various length of upstream and downstream sections. Also, three different velocity profile has prescribed at inflow plane. The distribution near ramp section is shown in zoom in plot.

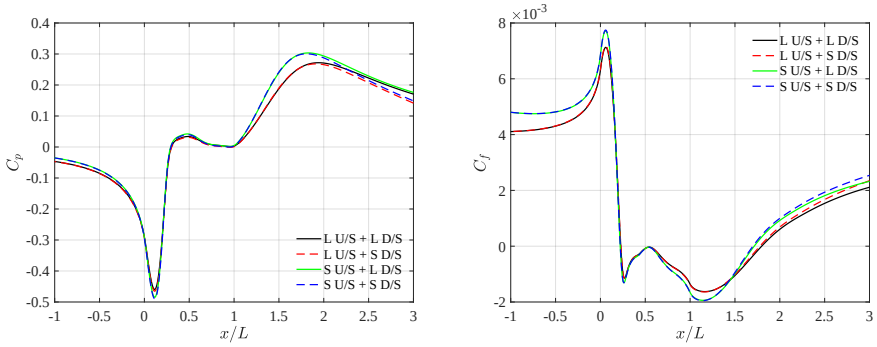

(a) Uniform velocity inlet profile

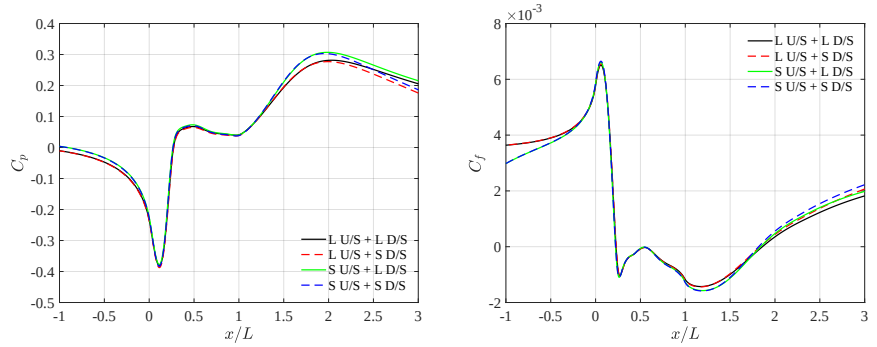

(b) Blasius velocity inlet profile

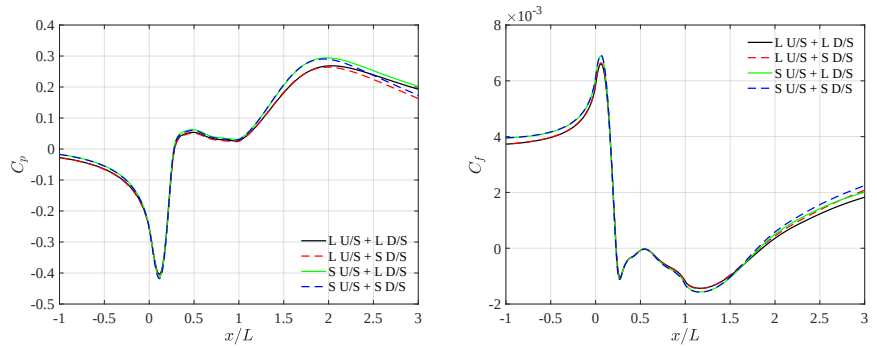

(c) Turbulent velocity inlet profile

Figure 3.8: Pressure and skin friction coefficient distribution along the curved wall (NASA1, $h/L = 0.4$, zoomed in at ramp section). The computational domain has a common ramp section and various length (L: long; S: short) of upstream (U/S) and downstream (D/S) sections. Also, three different velocity profile has prescribed at inflow plane.

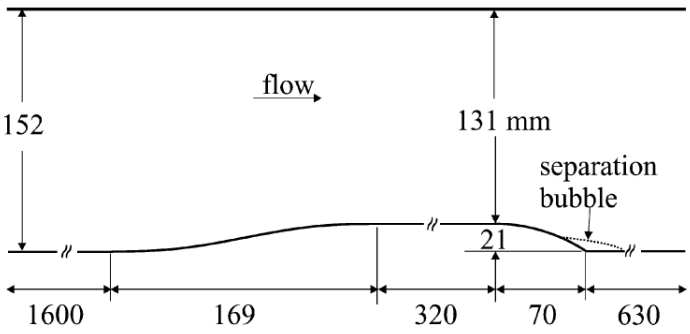

Figure 3.9: Flow schematic (Song and Eaton [2004])

to the onset of ramp. In the adverse pressure gradient region, the boundary layer thickness grows rapidly and hence there is a decrease in C_f. The two minimum values $C_{f_{\min}}$ and flat section of C_p around $x/L = 1$ are related to the structure of the recirculation region. After separation, the detached flow over the separation bubble impinges upon the downstream wall at reattachment and hence leads to an increase in C_f. This increase shows a slower recovery compared to the experimental data and LES result, which is typical for the Spalart-Allmaras model (Menter [1996]).

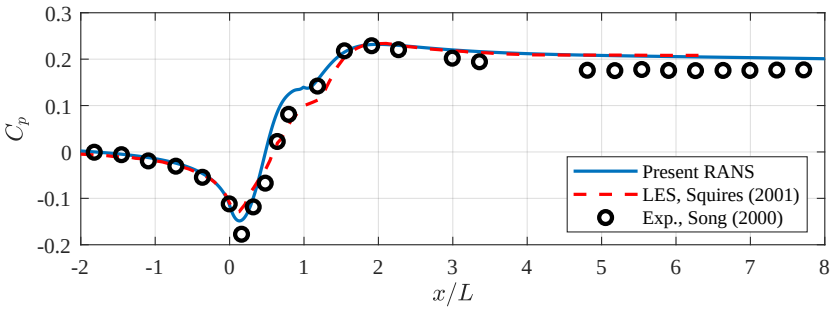

Figure 3.10: Comparison of static pressure coefficient along the curved wall. The reference station for static pressure is defined at $x/L = -1.81$.

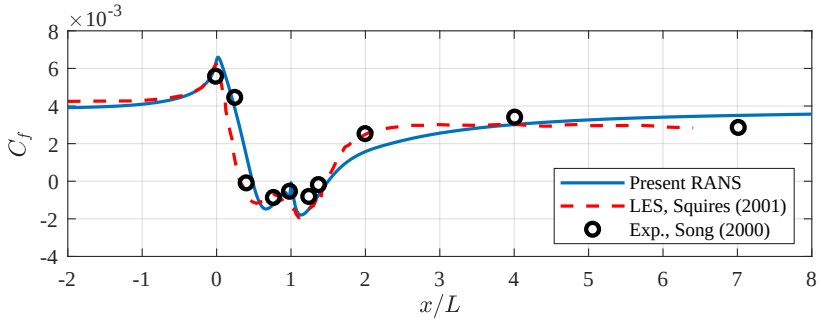

Figure 3.11: Comparison of skin friction coefficient along the curved wall.

Chapter 4

CRITERION FOR INCIPIENT SEPARATION OF TURBULENT FLOWS

In this chapter, we investigate the phenomenon of flow separation over various curved ramps and study the effects of the ramp geometry and inflow parameters. We wish to establish a purely geometric criterion for the incidence of incipient separation of turbulent flow over curved ramps.

4.1 Effects of ramp slope and curvature on C_f and C_p

4.1.1 Ramp geometry

A smooth ramp geometry, that is, a profile with zero first and second derivatives at the two end points is desired at the transition between the upstream and downstream flat sections. These derivatives are related to ramp slope, z', and curvature, κ, respectively. These two parameters are defined as

$$z' = \frac{dz}{dx}, \tag{4.1}$$

$$\kappa = \frac{-z''}{\left[1 + (z')^2\right]^{3/2}}. \tag{4.2}$$

As the ramp height keeps decreasing from the onset of ramp ($x/L = 0$) to the end of ramp ($x/L = 1$), the slope is always non-positive value. For convenience, all the plots involving slope use $-z'$. Also, the negative sign in Equation (4.2) is given to ensure convex curvature has a positive value.

We considered two categories of curved ramp geometries, which are modifications of the NASA afterbody profile of Disotell and Rumsey [2017] and a half-Gaussian geometry.

The first group of ramps has the same maximum curvature $\kappa_{\max}$ occurring at different streamwise locations, which is obtained by modifying the orders of polynomial function that defines the NASA afterbody geometry as shown in Figure 4.1. The second group consists of ramps with different $\kappa_{\max}$ magnitudes at same location and is achieved by modifying the Gaussian geometry as shown in Figure 4.2. To achieve this, the Gaussian ramp was cutoff at a certain length and scaled to

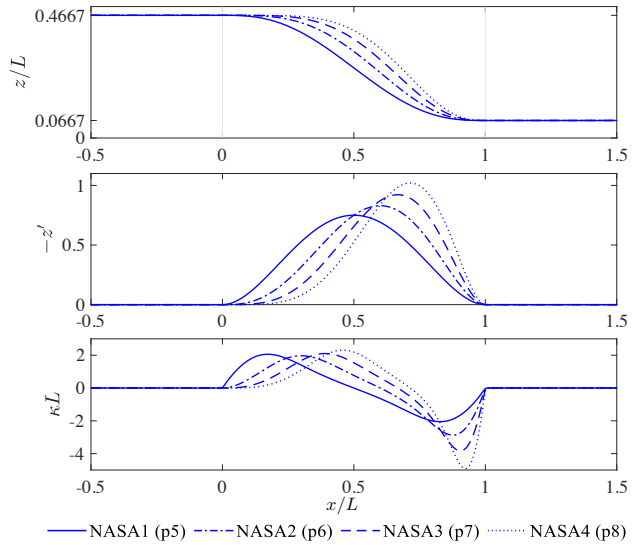

Figure 4.1: Geometric property of NASA ramp group. NASA1 is the original NASA ramp, NASA2-4 are obtained by modifying of the orders of polynomial function. For a given h/L, $-z'_{max}$ and κ_{min} increases monotonically, and $\kappa_{\max}$ remain at the same level.

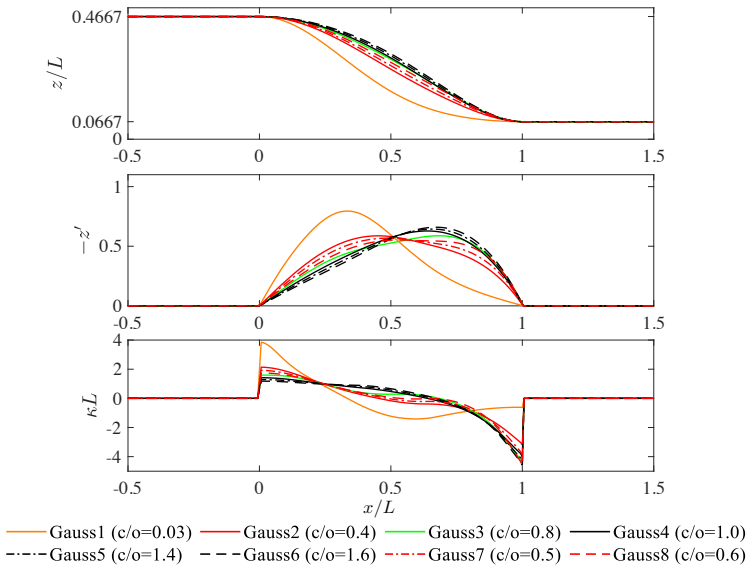

Figure 4.2: Geometric property of Gaussian ramp group. The slope distribution is diverse by using different cutoff values. For a given h/L, $\kappa_{\max}$ remain at the same streamwise location (near the onset of ramp) but different magnitudes.

the desired ramp length L. For all Gaussian ramp geometries we use $s = 1.5$, with various cutoff thresholds, $0.03, 0.4, 0.8$.

In order to avoid any discontinuity between the end of Gaussian ramp and downstream flat section, quintic spline interpolation was used. This spline interpolation improves the smoothness of the ramp which guarantees a continuous slope distribution and a milder jump in the curvature at the end of the ramp.

In addition to the NASA and Gaussian ramps, two more ramp geometries are introduced: DARPA suboff geometry given by Groves et al. [1989] and an error function (ERF) ramp. The ERF ramp consists of quintic spline at both ends of the ramp. All the ramp profiles are defined in Table 4.1.

4.1.2 Effect of ramp height-to-length ratio (h/L)

Figure 4.3 shows the minimum values of C_f for different values of the ramp height-to-length ratio h/L.

Critical ramp height

Theoretically, there is always a critical ramp height denoted by h_{crit}, where flow has an incipient separation point on the ramp, $C_{f_{\min}} = 0$. This critical ramp height can be obtained by using a third order polynomial curve fitting (see Figure 4.4). Closer inspection of Figure 4.3 shows that at the same h/L, the flow differently for different ramp geometries. For instance, at the critical ramp height of NASA2 $h_{crit,\text{NASA2}}$ (gray vertical line at $h/L \approx 0.14$ in Figure 4.3(a)), flow over NASA1 ramp is attached, while flow over NASA3 ramp is separated. The geometrical effects on the three flow regimes of attached, incipient separation and separated flows are discussed in the next section.

4.1.3 Effects of slope and curvature distribution

Figures 4.5 $\sim$ 4.10 show the ramp profile z/L, slope $-z'$, curvature κL, C_p, pressure gradient dC_p/dx, and C_f for three values of $h/L = 0.0333$, 0.1431 for NASA or 0.1902 for Gaussian, 0.4 for each geometry. The δ_0/L and Re_L for these cases are 1/25 and $Re_L = 200,000$ respectively. The three h/L cases represent attached flow $h/L = 0.0333$, incipient separation $h/L = 0.1431$ for NASA

Ramp profile	Definition
NASA1	$z(x) = h_u + h_u\,(1-\sigma)\left(-\dfrac{10x^3}{L^3} + \dfrac{15x^4}{L^4} - \dfrac{6x^5}{L^5}\right)$
NASA2	$z(x) = h_u + h_u\,(1-\sigma)\left(-\dfrac{15x^4}{L^4} + \dfrac{24x^5}{L^5} - \dfrac{10x^6}{L^6}\right)$
NASA3	$z(x) = h_u + h_u\,(1-\sigma)\left(-\dfrac{21x^5}{L^5} + \dfrac{35x^6}{L^6} - \dfrac{15x^7}{L^7}\right)$
NASA4	$z(x) = h_u + h_u\,(1-\sigma)\left(-\dfrac{28x^6}{L^6} + \dfrac{48x^7}{L^7} - \dfrac{21x^8}{L^8}\right)$
Gaussian	$z(x) = h_d + h\exp\left(-\dfrac{x^2}{s}\right)$
DARPA	$z(\xi) = h_u\left[{h_d}^2 + h_d K_0 \xi^2 + \left(20 - 20{h_d}^2 - 4h_d K_0 - \dfrac{1}{3}K_1\right)\xi^3 + \left(-45 + 45{h_d}^2 + 6h_d K_0 + K_1\right)\xi^4 + \left(36 - 36{h_d}^2 - 4h_d K_0 - K_1\right)\xi^5 + \left(-10 + 10{h_d}^2 + h_d K_0 + \dfrac{1}{3}K_1\right)\xi^6\right]^{1/2}$
ERF	$z(x) = \dfrac{h_u - h_d}{2}\left[\mathrm{erf}\left(-\dfrac{x - L/2}{2}\right) + 1\right] + h_d$

Table 4.1: Definitions of the NASA, Gaussian, DARPA and ERF ramp. In the above definitions, h_u is the height of the upstream flat setion, h_d is the height of the downstream flat section, $\sigma = h_d/h_u$, h is the ramp height and L is the ramp length (see Figure 2.3). In the case of the DARPA ramp, $h_d = 0.1175$, $K_0 = 10$, $K_1 = 44.6244$ and $\xi = (13.98 - x)\,/3.33$. For the Gaussian ramp, the slope $s = 1.5$. All the geometries are scaled into the common ramp height h and ramp length L.

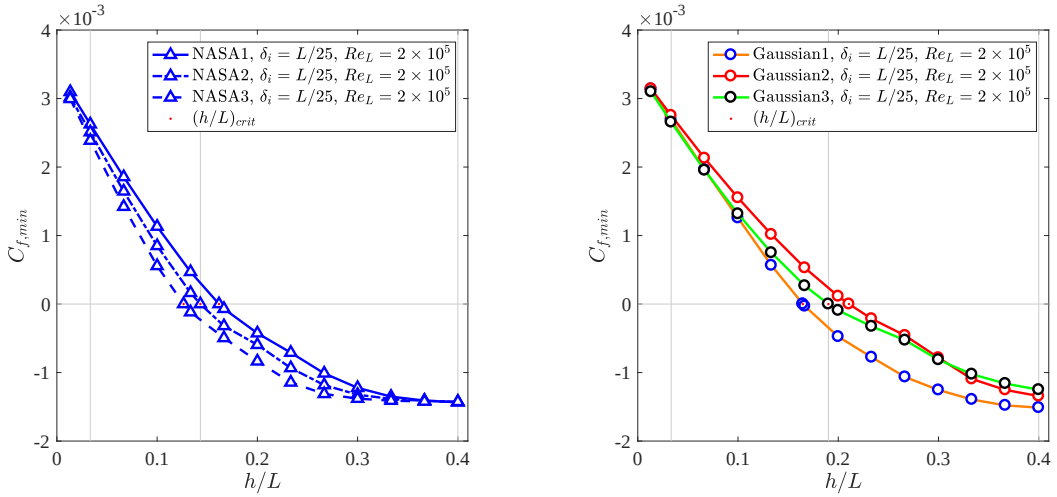

(a) (b)

Figure 4.3: h/L effect on flow separation. $\delta_i = L/25$. $Re_{\delta_i} = 8,000$; $Re_L = 2 \times 10^5$.

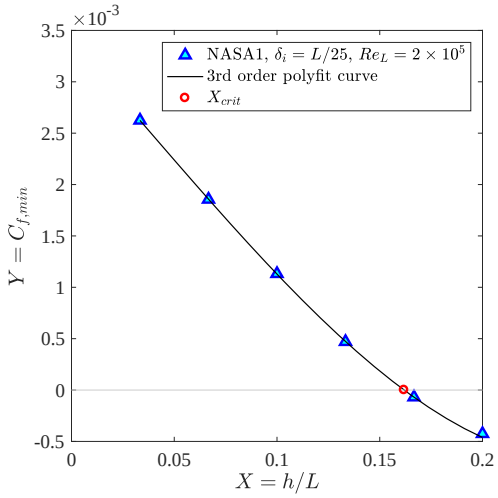

Figure 4.4: Minimum skin friction coefficient, $C_{f_{\min}}$, as a function of ramp height-to-length ratio, h/L. The black solid line is a third order polynomial curve fit to our data (NASA1 ramp geometry, $\delta_i = L/25$, $Re_L = 2 \times 10^5$). The expression of curve is $Y = 0.1716X^3 - 0.0179X^2 - 0.0225X + 0.0034$, and RMSE $= 4.4869 \times 10^{-6}$. The red circle represents the critical ramp height, h_{crit}.

or $h/L = 0.1902$ for Gaussian, and separated flow $h/L = 0.4$. It is interesting to note that the plots of slope and curvature exhibit the same behavior independent of the ramp height. Moreover, these plots illustrate the main characteristics of the relationship between ramp geometries and C_p, C_f.

1. C_p is negatively correlated with the curvature for attached flows (see Figures 4.5(c)(d) and Figures 4.8(c)(d)). As the ramp height increases, for the critical ramp and further when the flow separates, this correlation is still obvious in the first half of ramp ($x/L \in [0, 0.5]$) but not in the second half ($x/L \in [0.5, 1]$).

2. The favorable pressure gradient ($dC_p/dx < 0$) is correlated with the ramp curvature, however, the distribution of adverse pressure gradient ($dC_p/dx > 0$) reassembles the ramp slope.

3. C_f is correlated with the curvature in the region of favorable pressure gradient, however, it is correlated with slope in the region of adverse pressure gradient. This is can be seen in Gaussian plots where $C_{f_{\max}}$ location depends on the $\kappa_{\max}$ location.

4. Ramp curvature has a local effect on the C_f in the region of favorable pressure gradient near the onset of ramp.

5. Ramp slope affects the minimum of C_f, which correlated with both the incidence of flow separation and the separation point. As h/L increases, especially for fully separated flows, the minimum C_f moves toward the upstream. Flow separation occurs first in the ramp that reaches the critical slope.

4.2 Effects of Reynolds number and boundary layer thickness on C_f and C_p

In § 3.4, the effect of the upstream length is discussed in detail. We saw that a longer upstream section gives a thicker boundary layer thickness downstream. Increasing Reynolds number provides more inflow momentum, which can delay the flow separation.

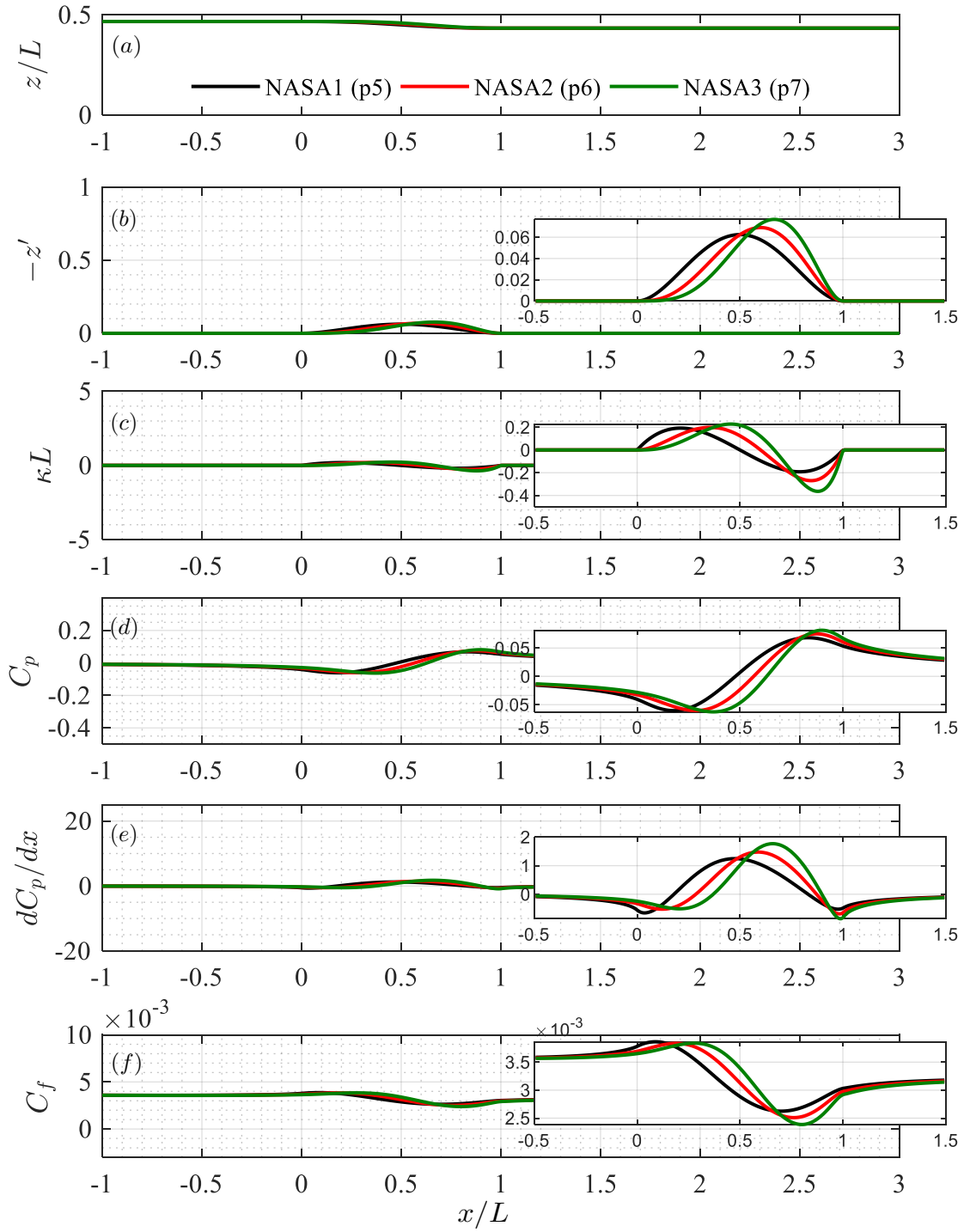

Figure 4.5: Effects of slope and curvature for NASA ramp ($h/L = 0.0333$) where flow is attached.

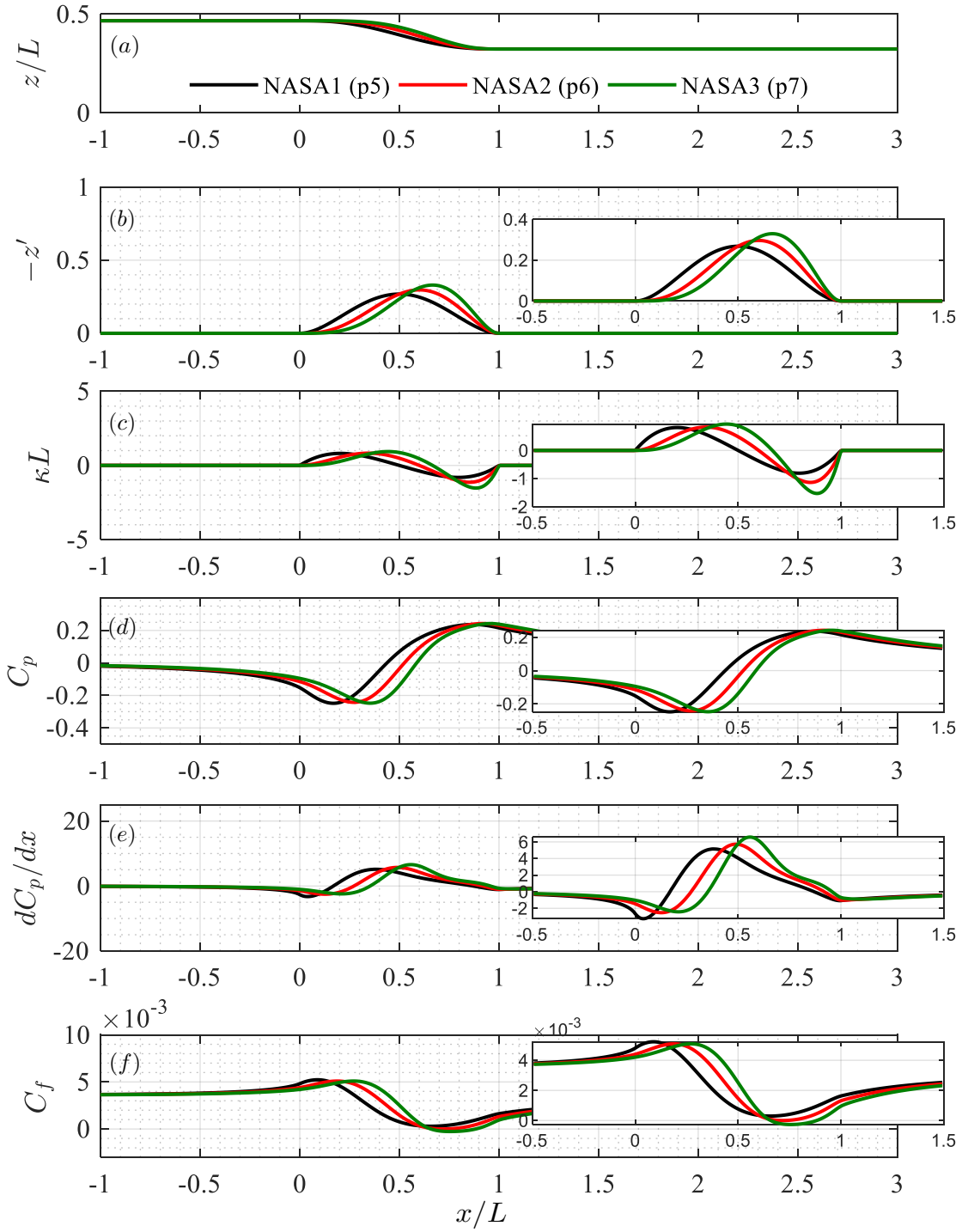

Figure 4.6: Effects of slope and curvature for NASA2 critical ramp ($h/L = 0.1431$).

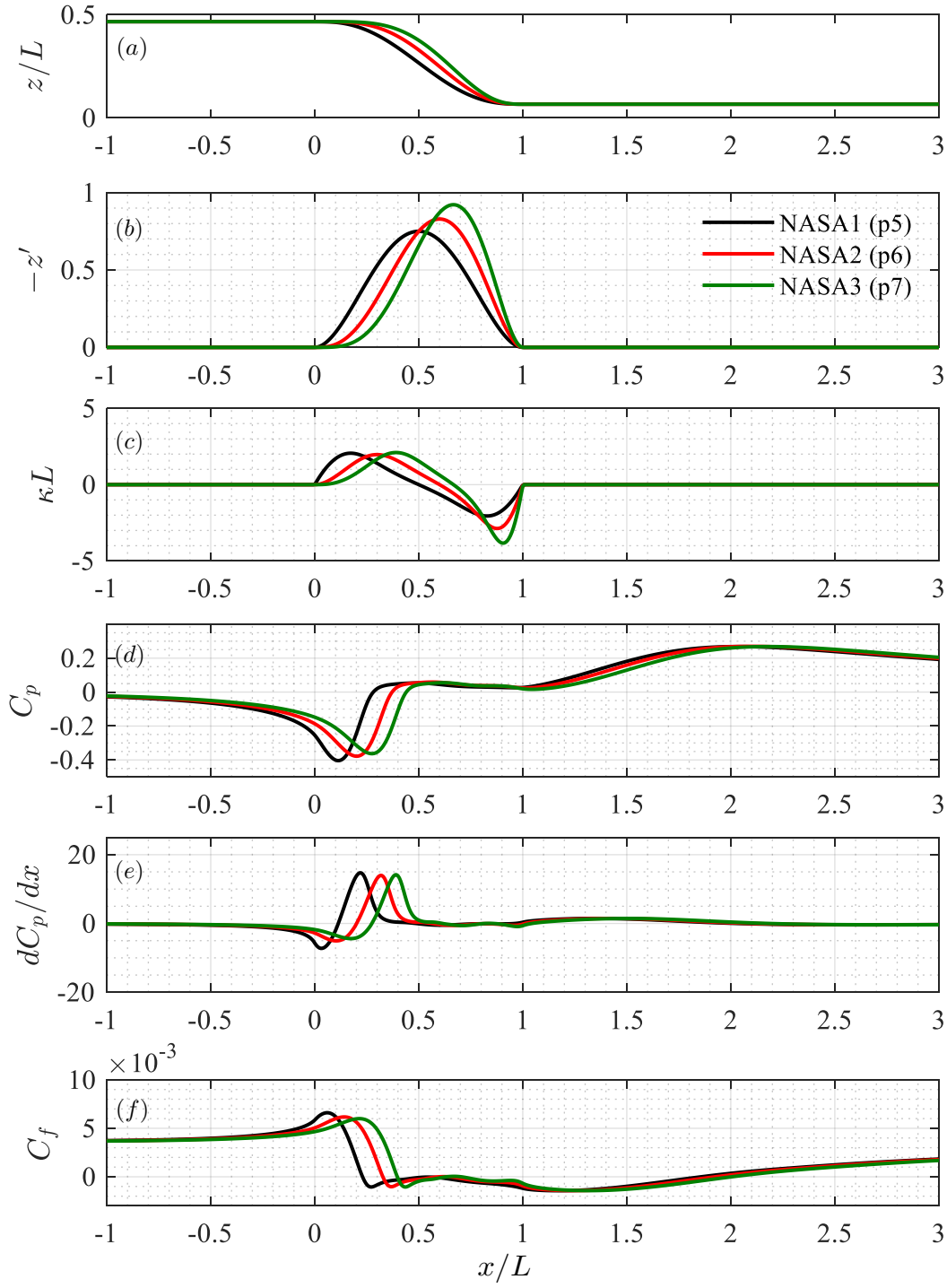

Figure 4.7: Effects of slope and curvature for NASA ramp ($h/L = 0.4$) where flow is separated.

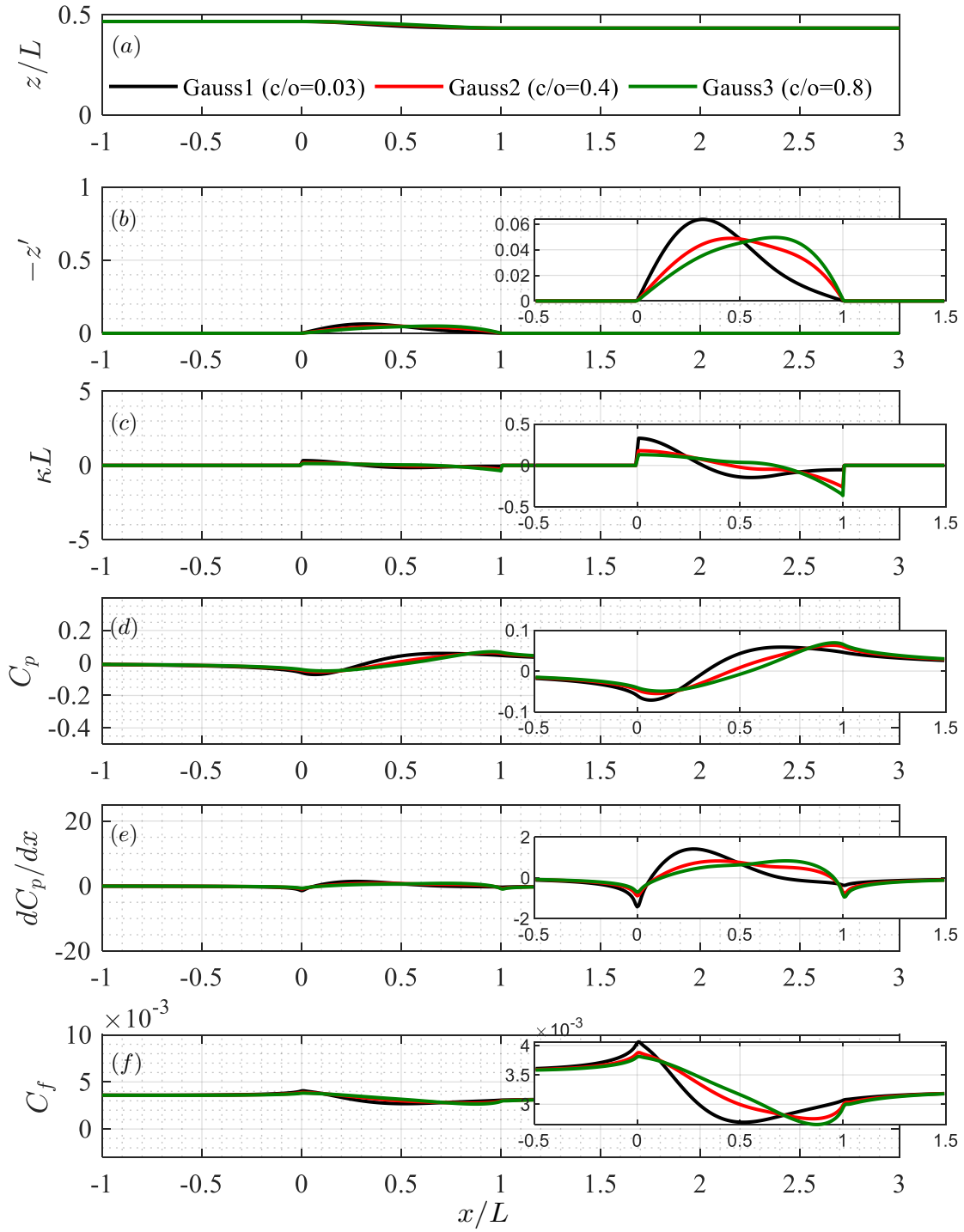

Figure 4.8: Effects of slope and curvature for Gauss ramp ($h/L = 0.0333$) where flow is attached.

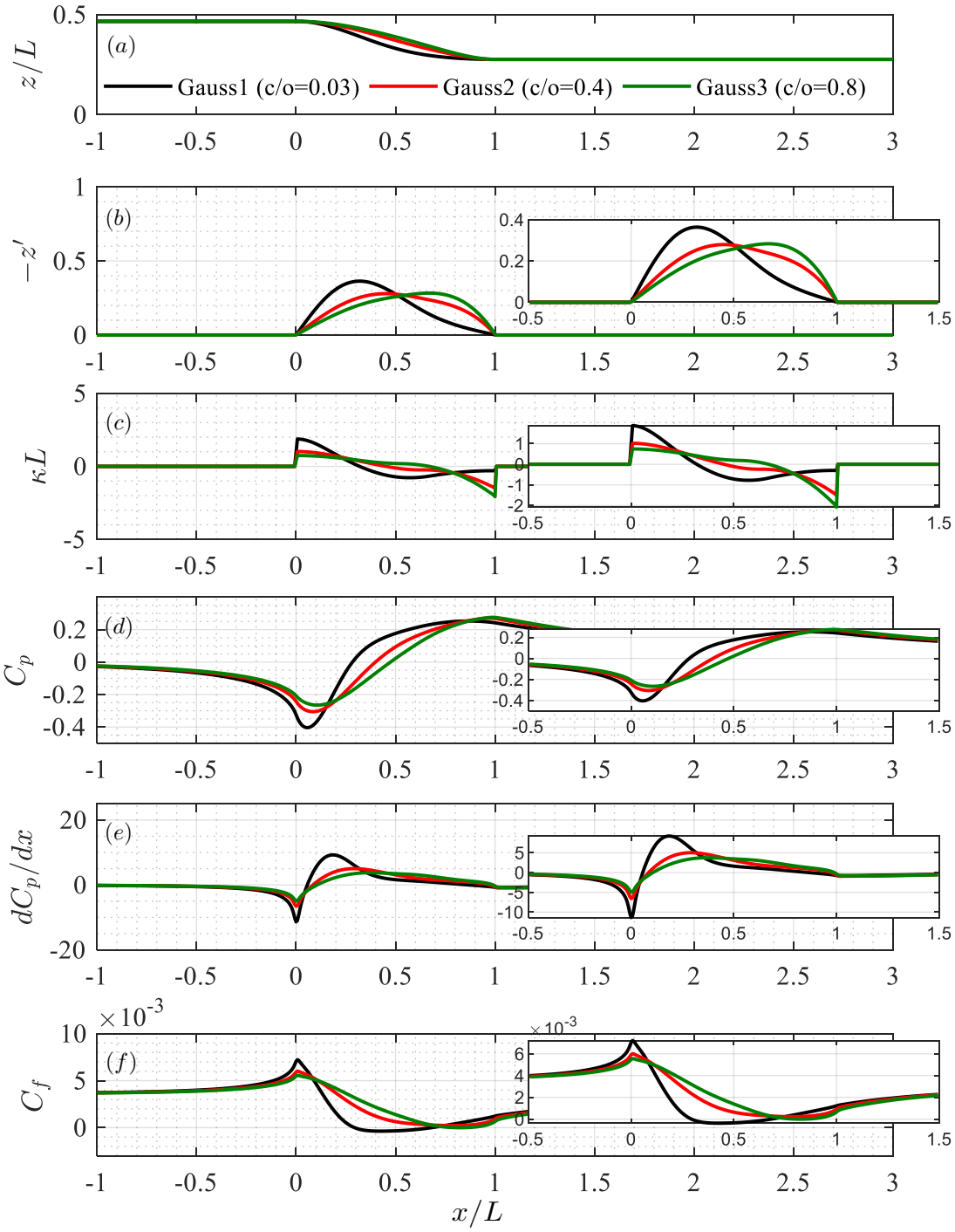

Figure 4.9: Effects of slope and curvature for Gauss2 critical ramp ($h/L = 0.1902$).

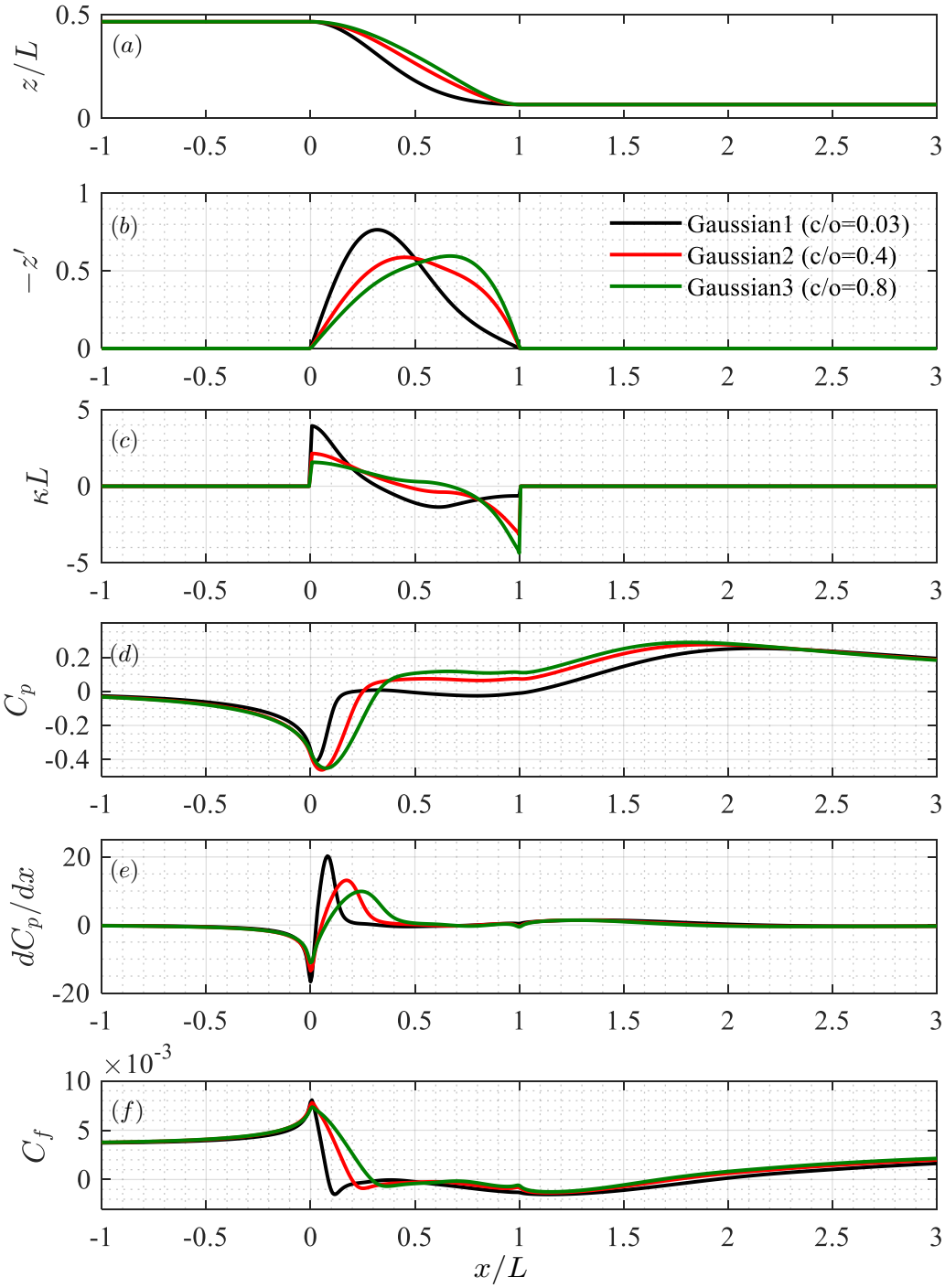

Figure 4.10: Effects of slope and curvature for Gauss ramp ($h/L = 0.4$) where flow is separated.

Case	$U_\infty\ (m/s)$	$\delta_i\ (mm)$	$\theta_i\ (mm)$	$\delta_i^*\ (mm)$	$Re_{\delta,i}$	$Re_{\theta,i}$	$Re_{\delta^*,i}$
NASA1Re1	11.6859	10	1.2	1.8	8,000	982.6	1455.9
NASA1Re2	23.3718	10	1.2	1.7	16,000	1908.5	2696.5
NASA1Re3	46.7435	10	1.2	1.6	32,000	3698.9	5052.1

Table 4.2: Flow conditions of test case with different Reynolds numbers at inflow location $x/L = -4$.

4.2.1 Reynolds number

Table 4.2 shows the flow conditions for the three test cases. Figure 4.11(a) shows the $C_{f_{\min}}$ as a function of the ramp height-to-length ratio h/L for three Reynolds numbers $Re_L = 2 \times 10^5,\ 4 \times 10^5,\ 8 \times 10^5$. In Figure 4.11(a), as Reynolds number increases, the critical ramp height increases as well. Therefore, flows with higher Reynolds numbers can stay attached over steeper ramps.

4.2.2 Boundary layer thickness (δ_i/L)

Calculation of the boundary layer thickness

The following procedure was developed to calculate boundary layer thickness for flow over curved wall since edge velocity of the boundary layer is not well defined. We omit the brackets $\langle \ldots \rangle$ for simplicity. We define the boundary edge as a streamline where the flow satisfies Bernoulli's Equation:

$$U_{\mathrm{sl}} \frac{dU_{\mathrm{sl}}}{ds_{\mathrm{sl}}} = -\frac{1}{\rho} \frac{dp_{\mathrm{sl}}}{ds_{\mathrm{sl}}} \tag{4.3}$$

where subscript sl indicates that the variables are computed along the streamline. The edge velocity, U_e, is defined by the velocity magnitude on the streamline. Then, the boundary layer thickness, δ, is given by the distance to the point along the wall normal direction (ζ) where the velocity magnitude (i.e., the streamwise velocity vector) reaches 99% of U_e. Furthermore, the momentum thickness θ and displacement thickness δ^* are defined as

$$\theta \equiv \int_0^\delta \left(1 - \frac{u}{U_e}\right) \frac{u}{U_e} d\zeta, \tag{4.4}$$

$$\delta^* \equiv \int_0^\delta \left(1 - \frac{u}{U_e}\right) d\zeta, \tag{4.5}$$

Case	$U_\infty\ (m/s)$	$\delta_i\ (mm)$	$\theta_i\ (mm)$	$\delta_i^*\ (mm)$	$Re_{\delta,i}$	$Re_{\theta,i}$	$Re_{\delta^*,i}$
NASA1Re1	11.6859	10	1.2	1.8	8,000	982.6	1455.9
NASA1Re1a	11.6859	5	0.64	1.0	4,000	510.1	814.3
NASA1Re1b	11.6859	2.5	0.33	0.6	2,000	266.7	481.5

Table 4.3: Flow conditions of test case with different boundary layer thicknesses at inflow location $x/L = -4$.

The shape factor is defined as

$$H \equiv \frac{\delta^*}{\theta}. \tag{4.6}$$

Effect of boundary layer thickness

Table 4.3 shows flow conditions for the test cases where the effect of inflow boundary layer thickness is investigated. Figure 4.11(b) shows the $C_{f_{\min}}$ as a function of the ramp height-to-length ratio h/L for three inflow boundary layer thicknesses $\delta_i = L/25,\ L/50,\ L/100$. In Figure 4.11(b), the effect of inflow boundary layer thickness is not as apparent as that of Reynolds number. For critical ramp, flow with thicker inflow boundary layer thickness can stay attached over more radical ramps.

4.3 Estimation of flow separation using criterion for incipient separation

4.3.1 Formulation of the criterion for incipient separation

As described in § 4.1, C_f is correlated with ramp slope in the region with adverse pressure gradient, where flow is prone to separate. To find a relationship between flow separation and the ramp slope, we considered one more NASA geometry (NASA4) and five more Gaussian geometries (Gauss4-Gauss8). The Gaussian ramps are generated by varying cutoff values as shown in Figure 4.12. These additional geometries give diverse slope and curvature distributions which are shown in Figure 4.12.

In the following analysis, we only examine the geometrical properties for critical ramps in order to formulate the criterion for incipient separation, for which it is convenient to define two non-dimensional variables: $\widetilde{h} = h/L$, non-dimensional ramp-height based on its length, and $\widetilde{z'}_{\max} =$

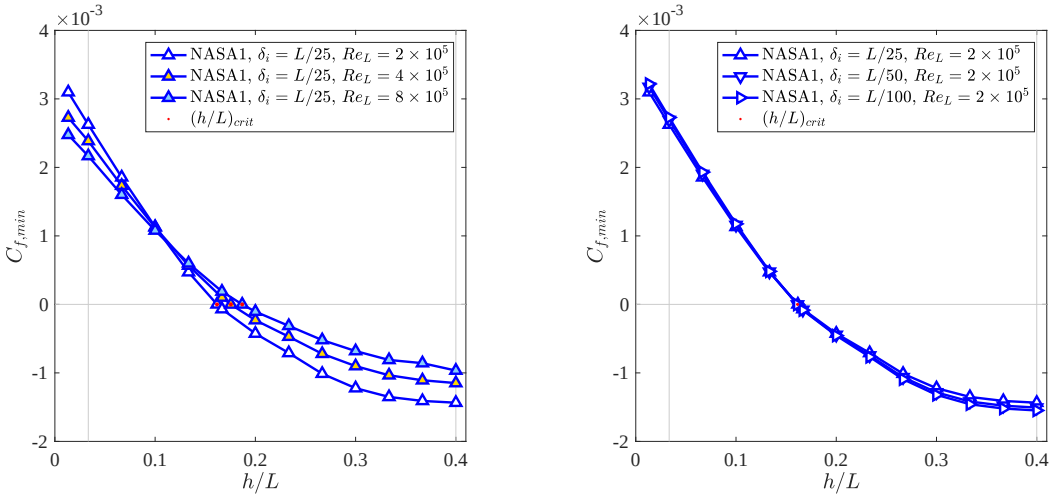

Figure 4.11: h/L effect on flow separation. $\delta_i = L/25$. $Re_{\delta_i} = 8,000$; $Re_L = 200,000$.

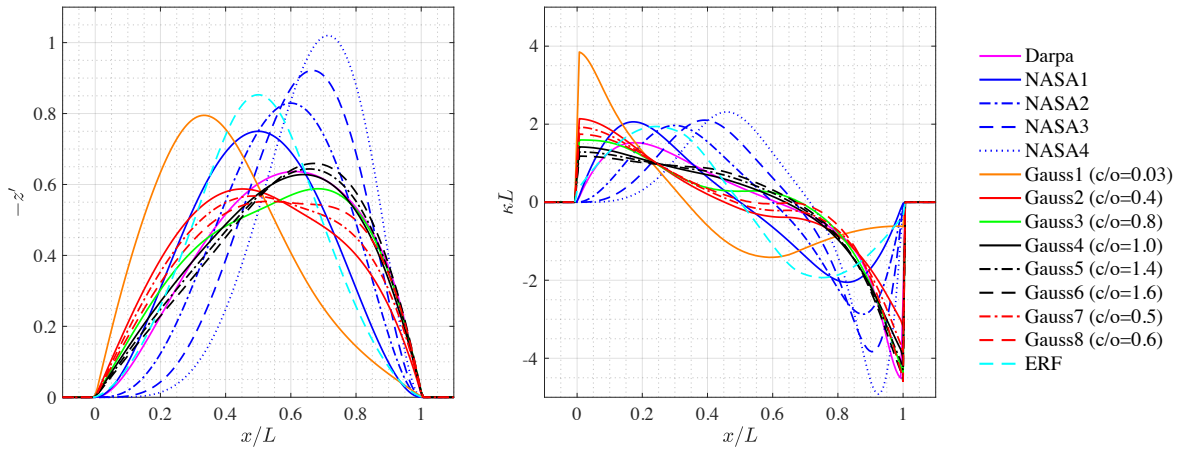

Figure 4.12: Current simulation matrix. Slope and curvature distribution of ramp $h/L = 0.4$.

$z'_{\max}/(h/L)$, ramp maximum slope normalized by $\widetilde{h}$.

Figure 4.13(a) shows the maximum slope of the critical ramps $-z'_{\text{crit,max}}$ of all the geometries considered as a function of the critical height-to-length ratio of the ramps $X = h_{\text{crit}}/L$. It can be seen that the geometries with similar slope distributions such as NASA1-4, Gaussian4-6, and Gaussian2,7,8 show linear translation in the critical plane $-z'_{\text{crit,max}}$ vs. h_{crit}/L. In order to find a criterion for all geometries, the slope is scaled by L/h_{crit} to obtain Y=$-z'_{\text{crit,max}}L/h_{\text{crit}}$. Figure 4.13(b) shows Y=$-z'_{\text{crit,max}}L/h_{\text{crit}}$ as a function of $X = h_{\text{crit}}/L$. A linear fit can be obtained for critical ramp of all geometries, thereby indicating the criterion for incipient separation for the curved ramps.

Following this, we expand from critical ramps to all the other ramps. After scaling the slope of all ramps by their ramp heights, and projecting onto the critical plane, all the ramps with attached flow lie on the left hand side of the fitted line, and all ramps with separated flow lie on its right as shown in Figure 4.14. We define this line as the criterion for incipient separation:

$$-\widetilde{z}'_{\text{crit,max}} = \alpha\widetilde{h} + \beta \tag{4.7}$$

where $\alpha = -11.82$, $\beta = 3.8$,

Therefore, given a ramp geometry, we can gauge whether the flow separates by using the following criterion:

$$\begin{cases} -\widetilde{z}'_{\max} > -\widetilde{z}'_{\text{crit,max}} \;\rightarrow\; \textit{Separated flow} \\ -\widetilde{z}'_{\max} < -\widetilde{z}'_{\text{crit,max}} \;\rightarrow\; \textit{Attached flow} \end{cases} \tag{4.8}$$

where $\widetilde{z}'_{\text{crit,max}}$ is defined in Equation (4.7).

To evaluate the accuracy and applicability of this criterion, the L_2 norm of the deviation of the sampled critical ramps from linear fit, σ, is calculated, and the gray band in Figure 4.14 and Figure 4.18 shows the band with width of 2σ. All the sampled critical ramps lie within the band except ramp Gauss2. The largest error of Gauss2 is probably due to the kinks in the curvature distribution at both end points of the ramp.

To verify this criterion, the error function ramp (ERF) is investigated. It should be noted that the ERF ramp was not used to find the criterion. It is seen in Figure 4.14 that the nature of flow over all ERF ramps are classified correctly. In addition, the critical ERF ramp lies on the line described by Equation (4.7).

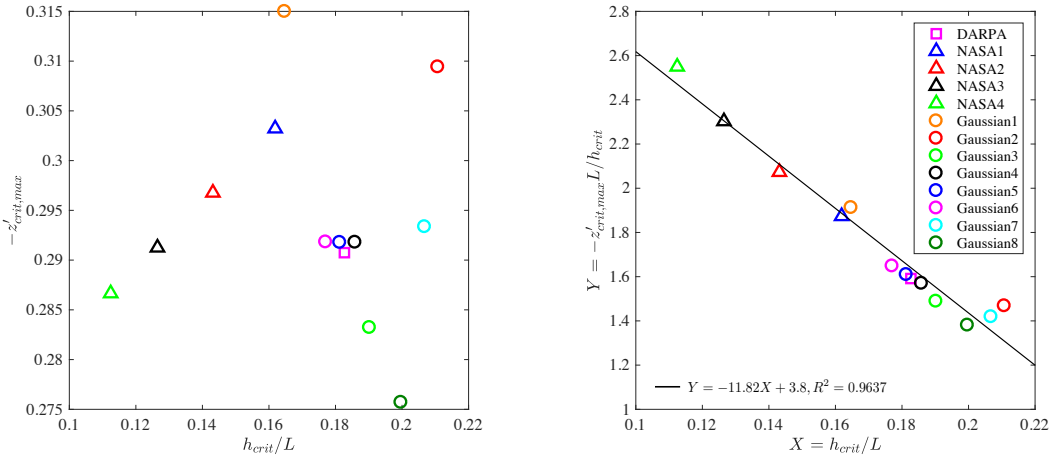

(a) (b)

Figure 4.13: The criterion of incipient separation. All cases shown in this plot are the critical ramp of each geometry. (a) Critical ramp height vs maximum slope of critical ramp. Linear relationship can be found for particular ramp groups but not for all. (b) Once Y is scaled by L/h_{crit}, all cases can be fitted by a single line.

Therefore, the flow separation of any given ramp can be estimated by locating it on phase diagram shown in Figure 4.15.

4.3.2 Reynolds number and boundary layer thickness dependence of criterion for incipient separation

Next, we study the effects of the Reynolds number and inlet boundary layer thickness. Figure 4.16(a) shows the maximum slope of the critical ramps $-z'_{\text{crit,max}}$ of all the geometries considered as a function of the critical height-to-length ratio of the ramps $X = h_{\text{crit}}/L$ at three Reynolds numbers $Re_L = 2 \times 10^5,\ 4 \times 10^5,\ 8 \times 10^5$. Firstly, it is seen that for different Reynolds numbers, all the points shift upward along the same direction. Figure 4.16(b) shows $-z'_{\text{crit,max}}L/h_{\text{crit}}$ as a function of h_{crit}/L for the three different Reynolds numbers $Re_L = 2 \times 10^5,\ 4 \times 10^5,\ 8 \times 10^5$. A linear fit can be obtained. Figure 4.16(b) shows that: 1) similar criteria are valid for larger Reynolds number; 2)

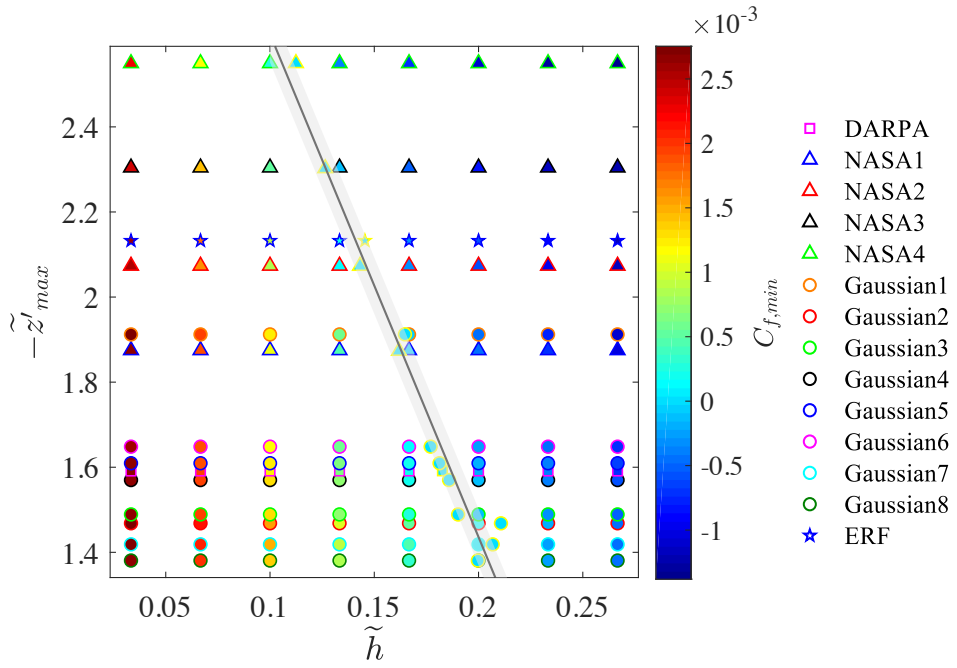

Figure 4.14: The black line is the criterion of incipient separation which is fitted by critical ramps denoted by yellow symbol edge color, and the gray band denotes 2σ region. All ramp geometries are distinguished: different symbols: ramp geometry category; different symbol edge colors: ramp geometry in each category. Symbol face color stands for the magnitude of $C_{f_{\min}}$. The ERF ramps are tested: critical ERF ramp lies on the criterion of incipient separation, and all other ramps belongs to the correct regions.

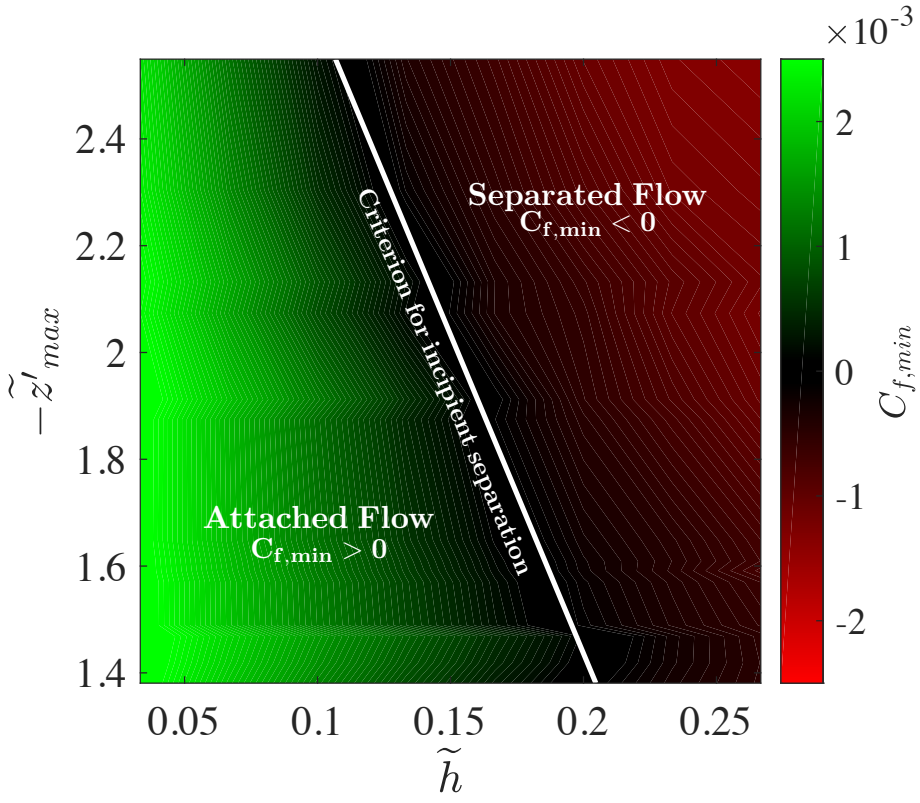

Figure 4.15: Phase diagram of turbulent boundary layer separation over smooth curved ramp. The white line indicates the boundary between positive and negative $C_{f_{\min}}$ alias, the criterion of incipient separation given by Equation (4.8).

a single common line can be fit by scaling X with a certain power of Re_L in order to yield the least fitting error as shown in Figure 4.16(c). It should be noted that the exponent of Reynolds number is 1/10, and hence the Reynolds number effect is weak for the incipient separation criterion in the range of Reynolds numbers presently considered.

Secondly, we vary the inflow boundary layer thickness to $\delta_i = L/25,\ L/50,\ L/100$, and all critical values collapse as shown in Figure 4.17. The separation between critical values for different boundary layer thicknesses is smaller than that of different Reynolds numbers. Therefore, we do not consider the effect of the inflow boundary layer thickness in the formulation of the criterion of incipient separation.

Finally, the criterion of incipient separation for $Re_L \in [2 \times 10^5, 8 \times 10^5]$, $\delta_i \in [L/25, L/100]$ is given as:

$$-\widetilde{z'}_{\text{crit,max}} = \alpha \widetilde{h} Re_L^{-1/10} + \beta \tag{4.9}$$

where $\alpha = -40.06$, $\beta = 3.8$.

Therefore, given a ramp geometry, we can gauge whether the flow separates by using the following criterion:

$$\begin{cases} -\widetilde{z'}_{\text{max}} > -\widetilde{z'}_{\text{crit,max}} \ \rightarrow \ \textit{Separated flow} \\ -\widetilde{z'}_{\text{max}} < -\widetilde{z'}_{\text{crit,max}} \ \rightarrow \ \textit{Attached flow} \end{cases} \tag{4.10}$$

where $\widetilde{z'}_{\text{crit,max}}$ is defined in Equation (4.9). The flow separation of any given ramp can be estimated by locating it on phase diagram shown in Figure 4.19.

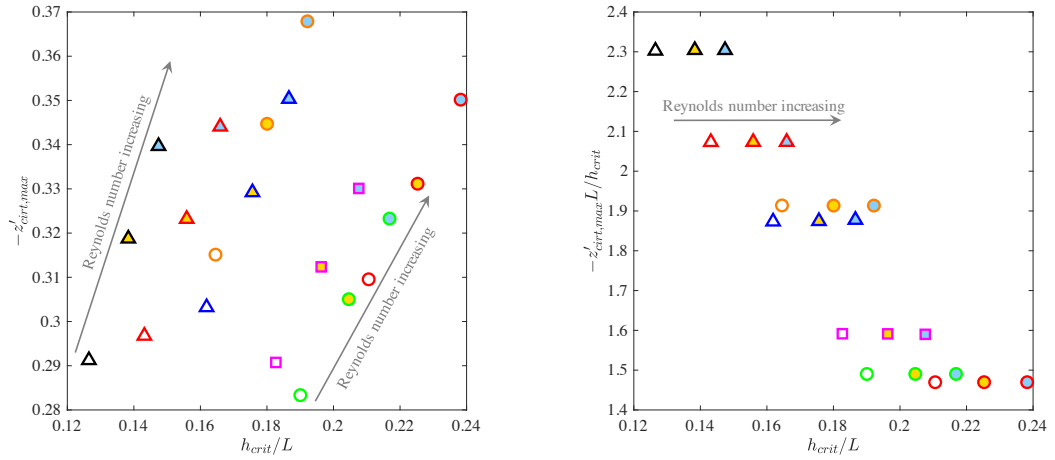

(a)

(b)

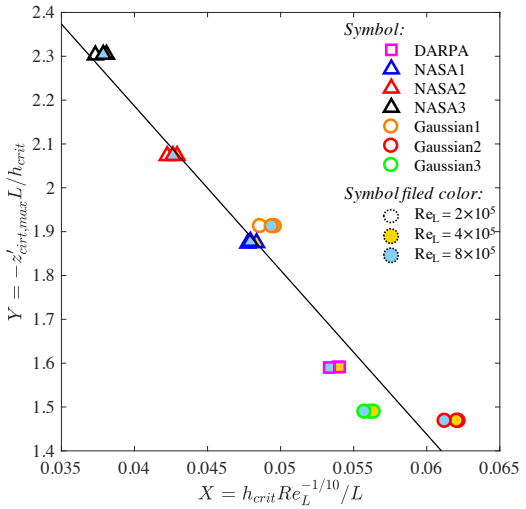

(c)

Figure 4.16: The criterion of incipient separation for higher Reynolds numbers. (a) Critical ramp height vs maximum slope of critical ramp. Linear relationship can be found for increased Reynolds number cases. (b) Once Y is scaled by L/h_{crit}, all cases for each Reynolds number can be fitted by a single line. (c) X is scaled by $Re_L^{-1/10}$ in order to find a line to fit the data points of all Reynolds number with the least error.

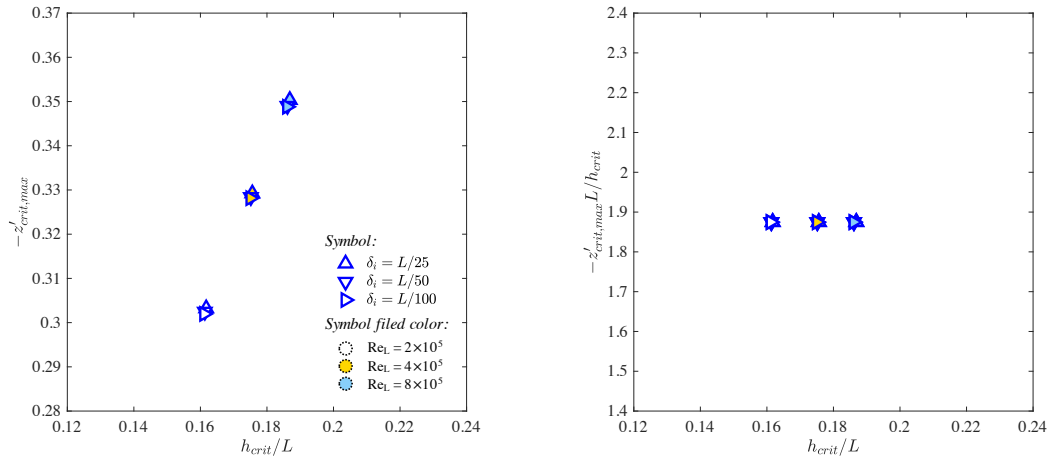

(a) (b)

Figure 4.17: The criterion of incipient separation for various inlet boundary layer thickness. For each Reynolds number, flow of three inlet boundary layer thicknesses over NASA1 ramp are examined. (a) Critical ramp height vs maximum slope of critical ramp. (b) three δ_i cases collapse when Y is scaled by L/h_{crit}. Comparing with Reynolds number effect, inlet boundary layer thickness has a weak relationship with incipient separation in current range of δ_i.

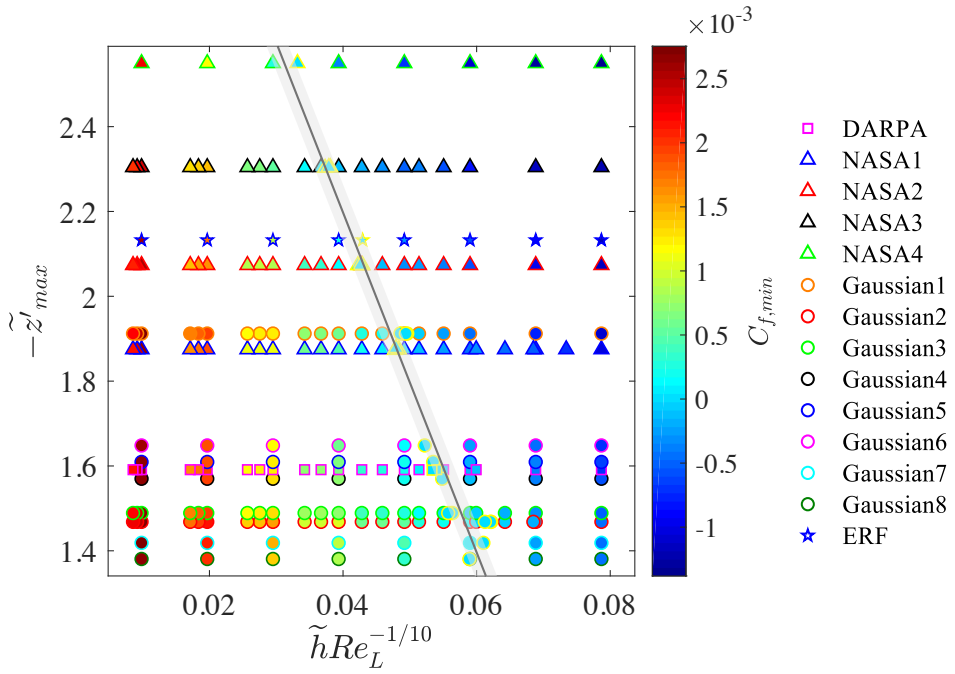

Figure 4.18: The black line is the criterion of incipient separation which is fitted by critical ramps denoted by yellow symbol edge color, and the gray band denotes 2σ region. All ramp geometries are distinguished: different symbols: ramp geometry category; different symbol edge colors: ramp geometry in each category. Symbol face color stands for the magnitude of $C_{f_{\min}}$. The ERF ramps are tested: critical ERF ramp lies on the criterion of incipient separation, and all other ramps belongs to the correct regions.

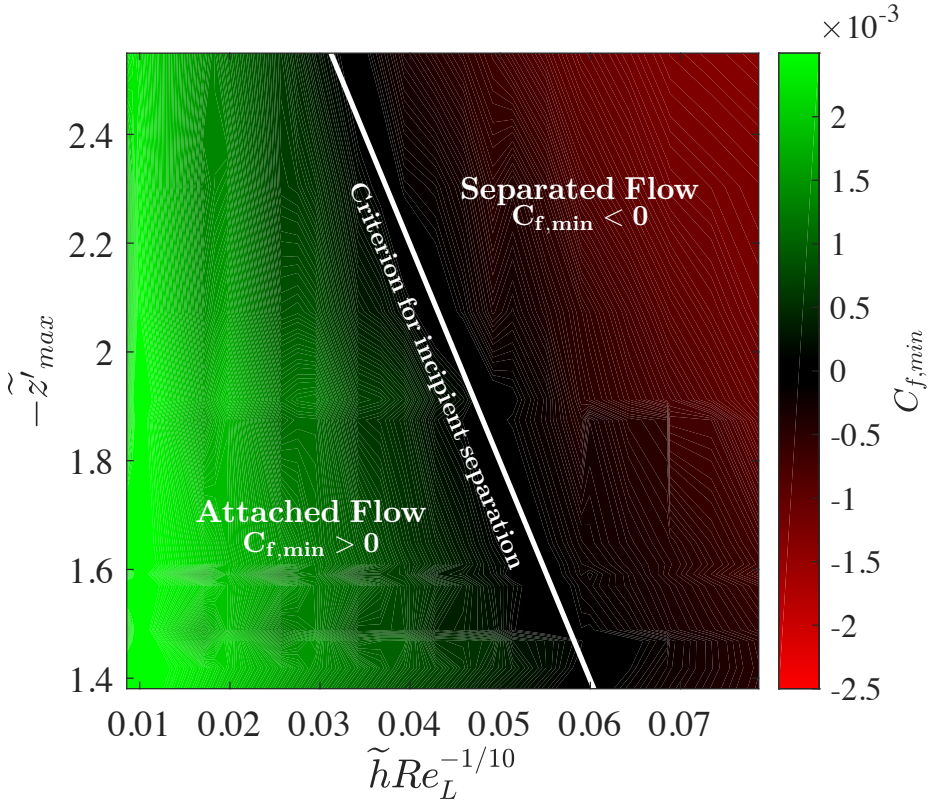

Figure 4.19: Phase diagram of turbulent boundary layer separation over smooth curved ramp for $2 \times 10^5 \leq Re_L \leq 8 \times 10^5$. The white line indicates the boundary between positive and negative $C_{f_{\min}}$, alias, the criterion of incipient separation given by Equation (4.10).

Chapter 5

SUMMARY

We performed RANS simulations of turbulent flows over curved ramps with adverse pressure gradient using the commercially available ANSYS Fluent flow solver. The RANS simulations performed did not use any wall-function models and the RANS equations were resolved in the viscous sublayer with the closest grid point to the wall located at $z^+_{\max} < 0.4$. We have accomplished two main goals: 1. we have established best practices to set up and run such RANS simulations; 2. we have also identified a simple criterion to estimate the occurrence of incipient separation of turbulent flows over curved ramps based solely on geometrical parameters and the Reynolds number of the flow. The main findings in the present thesis are:

- Best practices of RANS simulations have been discussed in detail. Wall resolved Spalart-Allmaras model with a proper combination of computational grid, domain size, and inlet boundary condition yield reliable estimation of flow separation. The proper upstream length of the domain should ensure that the inflow boundary layer has space to develop under zero pressure gradient. The downstream length provides sufficient space for the pressure to recover to satisfy the outflow boundary condition. Based on this study, the recommended values for the length of upstream and downstream sections are $4L$ and $9L$ respectively. The inflow velocity profile should be extracted from a flat plate turbulent boundary layer with the desired boundary layer thickness. Uniform velocity profile at the inflow plane requires a longer upstream length for the boundary layer to reach the desired boundary layer thickness. Also, the Blasius velocity profile has unphysical adjustment and is not recommended at the inflow plane.

- We have validated the flow solver and the best practices established above. C_f and C_p are in good agreement with the experimental data by Song and Eaton [2004].

- We investigated the effects on C_f and C_p of the ramp's slope and curvature by performing

RANS on different geometries for which we could vary the spatial distribution and magnitude of these two parameters independently. We found that while there is a correlation between the spatial distribution of studied ramp curvature and skin-friction coefficient near the onset of the ramp (favorable pressure gradient region), the key geometrical property for flow separation is the ramp slope.

- We found that the critical ramp heights of all ramp geometries studied obey a criterion for incipient separation. The criterion for incipient separation allows us to estimate whether flow separates over a given ramp by using only its geometrical property of h, L, and z'_{max}, and the Reynolds number, Re_L.

  The validity of this criterion is demonstrated in physical parameter range for which we performed RANS, i.e., $2 \times 10^5 \leq Re_L \leq 8 \times 10^5$ and $L/100 \leq \delta_i \leq L/25$. The dependence of the criterion on Reynolds number is weak ($Re_L^{-1/10}$) while it is unaffected by the inflow boundary layer thickness.

  This criterion could for example being used in aerodynamic design for establishing what is the maximum slope allowed to keep the flow attached for a given h/L (and Re_L).

As continuation of this work, we see the following opportunities:

1. derive a theoretical explanation for the validity of the criterion based on integral boundary layer equations;

2. extend of the criterion to high-Reynolds number flows;

3. extend of the criterion to axisymmetric body for airplane design applications.

BIBLIOGRAPHY

Brain G. Allan and Norman W. Schaeffler. Numerical investigation of rotorcraft fuselage drage reduction using active flow control. *AHS International 67th Annual Forum and Technology Display; 3-5 May 2011; Virginia Beach, VA; United States*, 2011.

Amy E Alving and HH Fernholz. Turbulence measurements around a mild separation bubble and downstream of reattachment. *Journal of Fluid Mechanics*, 322:297–328, 1996.

Fluent ANSYS Inc. Theory guide. *Ansys Inc.*

Yacine Bentaleb, Sylvain Lardeau, and Michael A Leschziner. Large-eddy simulation of turbulent boundary layer separation from a rounded step. *Journal of Turbulence*, (13):N4, 2012.

Ishmail B Celik, Urmila Ghia, Patrick J Roache, et al. Procedure for estimation and reporting of uncertainty due to discretization in cfd applications. *Journal of fluids Engineering-Transactions of the ASME*, 130(7), 2008.

David B De Graaff and John K Eaton. Reynolds-number scaling of the flat-plate turbulent boundary layer. *Journal of Fluid Mechanics*, 422:319–346, 2000.

P Dengel and HH Fernholz. An experimental investigation of an incompressible turbulent boundary layer in the vicinity of separation. *Journal of Fluid Mechanics*, 212:615–636, 1990.

Kevin J Disotell and Christopher L Rumsey. Design of an axisymmetric afterbody test case for cfd validation. In *23rd AIAA Computational Fluid Dynamics Conference*, page 3792, 2017.

WA El-Askary. Turbulent boundary layer structure of flow over a smooth-curved ramp. *Computers & Fluids*, 38(9):1718–1730, 2009.

A. Ferrante and S.E. Elghobashi. A robust method for generating inflow conditions for direct simulations of spatially-developing turbulent boundary layers. *Journal of Computational Physics*, (1):372 – 387, 2004. ISSN 0021-9991. doi: https://doi.org/10.1016/j.jcp.2004.01.016.

Christer Fureby, Shuang Zhu, and David Jones. Large eddy simulation of the flow over a contoured ramp. In *TSFP DIGITAL LIBRARY ONLINE*. Begel House Inc., 2015.

Nancy C Groves, Thomas T Huang, and Ming S Chang. Geometric characteristics of darpa (defense advanced research projects agency) suboff models (dtrc model numbers 5470 and 5471). Technical report, DAVID TAYLOR RESEARCH CENTER BETHESDA MD SHIP HYDROMECHANICS DEPT, 1989.

M Hammache, FK Browand, and RF Blackwelder. Whole-field velocity measurements around an axisymmetric body with a stratford–smith pressure recovery. *Journal of Fluid Mechanics*, 461: 1–24, 2002.

FR Menter. A comparison of some recent eddy-viscosity turbulence models. *Journal of Fluids Engineering*, 118(3):514–519, 1996.

VC Patel and F Sotiropoulos. Longitudinal curvature effects in turbulent boundary layers. *Progress in Aerospace Sciences*, 33(1-2):1–70, 1997.

Stephen B Pope. *Turbulent flows*. Cambridge University Press, 2003.

S Radhakrishnan, U Piomelli, A Keating, and A Silva Lopes. Reynolds-averaged and large-eddy simulations of turbulent non-equilibrium flows. *Journal of Turbulence*, (7):N63, 2006.

Patrick J Roache. Perspective: a method for uniform reporting of grid refinement studies. *Journal of Fluids Engineering*, 116(3):405–413, 1994.

Christopher Rumsey, Thomas Gatski, William Sellers, Veer Vatsa, and Sally Viken. Summary of the 2004 cfd validation workshop on synthetic jets and turbulent separation control. In *2nd AIAA Flow Control Conference*, page 2217, 2004.

Christopher L Rumsey and Philippe R Spalart. Turbulence model behavior in low reynolds number regions of aerodynamic flowfields. *AIAA journal*, 47(4):982–993, 2009.

Roger L Simpson. Turbulent boundary-layer separation. *Annual Review of Fluid Mechanics*, 21(1): 205–232, 1989.

Jeffrey Slotnick, Abdollah Khodadoust, Juan Alonso, David Darmofal, William Gropp, Elizabeth Lurie, and Dimitri Mavriplis. Cfd vision 2030 study: a path to revolutionary computational aerosciences. 2014.

Simon Song and John K Eaton. Reynolds number effects on a turbulent boundary layer with separation, reattachment, and recovery. *Experiments in fluids*, 36(2):246–258, 2004.

P. Spalart and S. Allmaras. A one-equation turbulence model for aerodynamic flows. *30th Aerospace Sciences Meeting and Exhibit*, Jan 1992. URL `http://dx.doi.org/10.2514/6.1992-439`.

Philippe R Spalart and Christopher L Rumsey. Effective inflow conditions for turbulence models in aerodynamic calculations. *AIAA journal*, 45(10):2544–2553, 2007.

BS Stratford. The prediction of separation of the turbulent boundary layer. *Journal of fluid mechanics*, 5(1):1–16, 1959.

B Wasistho and KD Squires. Prediction of turbulent separation over a backward-facing smooth ramp. *Journal of Turbulence*, (6):N1, 2005.

Bono Wasistho and Kyle D Squires. Numerical investigation of the separated flow over a smoothly contoured ramp. *Proceedings of the Second Intl Sympos. on Turbulence and Shear Flow Phenomena*, 2001.

Frank M White and Isla Corfield. *Viscous fluid flow*, volume 3. McGraw-Hill New York, 2006.

Freddie D Witherden and Antony Jameson. Future directions in computational fluid dynamics. In *23rd AIAA Computational Fluid Dynamics Conference*, page 3791, 2017.

Appendix A

USER DEFINED FUNCTION (UDF) OF TOP BOUNDARY CONDITION

At top of the domain, a free shear boundary condition is implemented by using UDF. The UDF shown below copies the boundary cells center value into boundary face center value, so that the gradient at the boundary is zero.

```
# include "udf.h"
// u-velocity neumann boundary condition
DEFINE_PROFILE(u_neumann,t,i)
{
real xf[ND_ND], xc[ND_ND];
face_t f;
cell_t c0;
Thread *t0;

begin_f_loop(f,t)
{
F_CENTROID(xf,f,t);
c0 = F_C0(f,t);
t0 = THREAD_T0(t);
C_CENTROID(xc,c0,t0);
F_PROFILE(f,t,i) = C_U(c0,t0);
}
end_f_loop(f,t)
}

// v-velocity neumann boundary condition
DEFINE_PROFILE(v_neumann,t,i)
{
real xf[ND_ND], xc[ND_ND];
face_t f;
cell_t c0;
Thread *t0;
begin_f_loop(f,t)
{
```

```
30      F_CENTROID(xf,f,t);
31      c0 = F_C0(f,t);
32      t0 = THREAD_T0(t);
33      C_CENTROID(xc,c0,t0);
34      F_PROFILE(f,t,i) = C_V(c0,t0);
35      }
36      end_f_loop(f,t)
37      }
```

Appendix B

ANSYS FLUENT JOURNAL FILE FOR RANS SIMULATION

A journal file contains a sequence of ANSYS Fluent commands, and its purpose is to automate a series of commands and run on cluster.

Here is a typical journal file for the case of Gaussian8 ramp, $Re_L = 4 \times 10^5$, $\delta_i = L/25$.

```
/file/import/plot3d/mesh/ "grid-gauss-2001x255-init-o-gam-44-36-30_075_625-scale-ha-1_75-co-0_6-spl.grd"
/mesh/scale 0.0333333333333333 0.0333333333333333
/define/models/viscous/spalart-allmaras yes
/define/models/viscous/curvature-correction yes

/mesh/modify-zones/zone-type 1 fluid
/define/boundary-conditions/modify-zones sep-face-zone-angle 2 89 yes

/define/boundary-conditions/modify-zones zone-name 2 wall
/define/boundary-conditions/modify-zones zone-name 5 inlet
/define/boundary-conditions/modify-zones zone-name 6 outlet
/define/boundary-conditions/modify-zones zone-name 7 top
/define/boundary-conditions/modify-zones zone-type 7 velocity-inlet
/define/user-defined/interpreted-functions "parallel_udf_63_center.c" "cpp" 10000 no

/file/read-profile "tbl26g6_255_d0_01_t5_re2.prof"

/define/boundary-conditions/modify-zones zone-type 6 pressure-outlet
/define/boundary-conditions/set/pressure-outlet outlet () ke-spec no no yes turb-viscosity-ratio no 0.21044
     q

/define/boundary-conditions/modify-zones zone-type 5 velocity-inlet
/define/boundary-conditions/set/velocity-inlet inlet () velocity-spec no yes

direction-0 yes no "delta_0_01_t5_re2" x-velocity
direction-1 yes no "delta_0_01_t5_re2" y-velocity
p-sup yes no "delta_0_01_t5_re2" pressure
ke-spec yes
nut yes no "delta_0_01_t5_re2" modified-viscosity
```

```
q

/define/boundary-conditions/modify-zones zone-type 7 velocity-inlet
/define/boundary-conditions/set/velocity-inlet top () velocity-spec no yes
direction-0 yes yes "udf" u_neumann
direction-1 yes yes "udf" v_neumann
turb-viscosity-ratio-profile no 0.21044 q

/solve/set/discretization-scheme nut 1
/solve/monitors/residual/convergence-criteria 1e-6 1e-6 1e-6 1e-6

/solve/initialize initialize-flow

/solve/initialize/compute-defaults velocity-inlet inlet
/solve/initialize initialize-flow yes

/report/reference-values/compute velocity-inlet inlet

/file/write-case-data "tcr193g6_14.cas.gz"

/define/user-defined/interpreted-functions "parallel_udf_63_center.c" "cpp" 10000 no
/solve/set/number-of-iterations 100000
/solve/iterate 100000

/file/write-case-data "tcr193g6_14_steady.dat.gz"

/define/models unsteady-2nd-order yes

/solve/set/p-v-coupling 22

/file/auto-save/data-frequency 10000
/file/auto-save/case-frequency/each-time
/file/auto-save/root-name "tcr193g6_14.gz"

/solve/set/time-step 1e-5
/solve/dual-time-iterate 100000 200

/file/write-case-data "tcr193g6_14_1s.dat.gz"

y
```